Received: 10 September 2017 | Accepted: 25 March 2018

DOI: 10.1111/jmg.12316

ORIGINAL ARTICLE

WILEY Journal of METAMORPHIC GEOLOGY

Ultrahigh-temperature osumilite gneisses in southern Madagascar record combined heat advection and high rates of radiogenic heat production in a long-lived high-*T* orogen

Robert M. Holder[1] | **Bradley R. Hacker**[1] | **Forrest Horton**[2] | **A. F. Michel Rakotondrazafy**[3]

[1]Department of Earth Science, University of California, Santa Barbara, Santa Barbara, California

[2]Division of Geological and Planetary Sciences, California Institute of Technology, Pasadena, California

[3]Faculté des Sciences, Université d'Antananarivo, Antananarivo, Madagascar

Correspondence
Robert M. Holder, Department of Earth Science, University of California, Santa Barbara, Santa Barbara, CA.
Email: rholder@umail.ucsb.edu

Funding information
Division of Earth Sciences, Grant/Award Number: NSF-EAR-1348003; University of California, Santa Barbara, Grant/Award Number: NSF-EAR-1348003

Handling editor: Doug Robinson

Abstract

We report the discovery of osumilite in ultrahigh-temperature (UHT) metapelites of the Anosyen domain, southern Madagascar. The gneisses equilibrated at ~930°C/0.6 GPa. Monazite and zircon U–Pb dates record 80 Ma of metamorphism. Monazite compositional trends reflect the transition from prograde to retrograde metamorphism at 550 Ma. Eu anomalies in monazite reflect changes in fO_2 relative to quartz–fayalite–magnetite related to the growth and breakdown of spinel. The ratio Gd/Yb in monazite records the growth and breakdown of garnet. High rates of radiogenic heat production were the primary control on metamorphic grade at the regional scale. The short duration of prograde metamorphism in the osumilite gneisses (<29 ± 8 Ma) suggests that a thin mantle lithosphere (<80 km) or advective heating may have also been important in the formation of this high-*T*, low-*P* terrane.

KEYWORDS

heat advection, Madagascar, osumilite, radiogenic heat production, ultrahigh-temperature metamorphism

1 | INTRODUCTION

Granulite facies and ultrahigh-temperature metamorphism (UHTM: >900°C in the granulite facies) represent the thermal limit of processes within the Earth's crust (Kelsey & Hand, 2015). Due to the large volumes of granitic melt that can be generated during UHTM (Bea, 2012), understanding how UHT terranes form is fundamental to understanding (1) how crust differentiates (Sawyer, Cesare, & Brown, 2011) and (2) how lithosphere is weakened during (Nelson et al., 1996) and strengthened after (Sandiford & McLaren, 2002; Sandiford, Mclaren, & Neumann, 2002) orogenesis. UHTM has been reported in Archean through Cenozoic rocks (Brown, 2006) and is thought to be occurring in the middle to lower crust of Tibet today (Hacker, Ritzwoller, & Xie, 2014; Hacker et al., 2000). Despite the ubiquity of UHTM in the geological record, the relative importance of processes that led to UHTM in individual terranes is often unclear.

Ultrahigh-temperature metamorphism has been attributed to advection of heat through asthenospheric upwelling, juvenile magmatism and/or lithospheric extension; these processes are inferred to occur in arcs and back-arcs (Bohlen, 1987; Brown, 2006; Kemp, Shimura, & Hawkesworth, 2007; Pownall, 2014; Sandiford & Powell, 1986). Rigorously assessing the role of these heat sources in ancient rocks is difficult because of their inherent transience. Direct support for advective heating comes from exposed UHT rocks in the still-active arc of Japan (Kemp et al., 2007) and UHT rocks associated with Miocene-to-Recent lithospheric extension in Indonesia (Pownall, 2014). Indirect support comes from UHTM inferred at depth from high

heat flow measurements in back-arcs and in continental crust undergoing extension (Hyndman, Currie, & Mazzotti, 2005; Sandiford & Powell, 1986).

Ultrahigh-temperature metamorphism can also occur from heat sources entirely internal to the crust. UHTM can occur as the result of prolonged (>40 Ma) thickening of crust with high concentrations of radioactive elements (U, Th and K: Bea, 2012; Clark et al., 2015; Horton, Hacker, Kylander-Clark, Holder, & Jöns, 2016; Jaupart, Mareschal, & Iarotsky, 2016). In this case, no high-*T* magmatism is required. Support for this hypothesis includes ongoing UHTM in the middle to lower crust of modern central Tibet (Hacker et al., 2000, 2014), long UHT durations (40–100 Ma, e.g. Harley, 2016), and an apparent correlation of UHTM with supercontinent amalgamation (Brown, 2006). UHTM might also occur as a result of strain heating in shear zones (Nabelek, Whittington, & Hofmeister, 2010; Whittington, Hofmeister, & Nabelek, 2009), but strain heating is generally thought to be incapable of causing regional UHTM on its own due to the anticorrelation between shear strength and temperature, the anticorrelation between shear strength and degree of melting, and the tendency for strain to be partitioned into weaker layers where strain heating is less effective (Clark, Fitzsimons, Healy, & Harley, 2011).

In this paper, we test the relative importance of advection and radiogenic heat production in the metamorphism of the Ediacaran–Cambrian Anosyen domain, southern Madagascar, with phase-equilibria modelling and monazite+zircon petrochronology. A correlation between terrane-scale radiogenic heat-production rate and metamorphic T/P indicates that the distribution of U, Th and K was a primary control on regional metamorphic grade. Thermal modelling suggests that average crustal heat-production rates must have been >3 μW/m³ and that the mantle lithosphere must have been relatively thin (<80 km) in order to explain the peak *P–T–t* conditions recorded by the gneisses: ~930°C/0.6 GPa, and prograde metamorphism over 20–40 Ma. Advection of heat by high-*T* magmatism may also have been important locally. Evidence supporting a component of advective heating includes: (1) the spatial coincidence of osumilite gneisses around the voluminous Anosyen Batholith, a batholith of high-*T* (mostly felsic) plutons, at least some of which were emplaced during prograde to peak metamorphism in the surrounding gneisses; (2) a short duration of prograde metamorphism (20–40 Ma) and (3) the low pressures (~0.6 GPa) inferred for prograde metamorphism.

2 | THE ANOSYEN DOMAIN OF SOUTHERN MADAGASCAR

The Anosyen domain (Figure 1) is the southeasternmost and highest grade tectonic unit of the Malagasy basement. It is bounded by the Androyen domain to the west and the Ikalamavony domain to the north. It is composed of metapelitic, calcsilicate and felsic paragneisses that were deposited in the Meso- to Neoproterozoic then metamorphosed and intruded by the Anosyen Batholith/Ambalavao suite between 590 and 510 Ma (e.g. GAF-BGR, 2008; Tucker, Roig, Moine, Delor, & Peters, 2014). Detrital zircon ages indicate that the Anosyen metasedimentary rocks are likely correlative with other metasedimentary rocks exposed throughout central and northern Madagascar, south India and Sri Lanka, suggesting a shared tectonic history of these regions prior to Ediacaran–Cambrian metamorphism (Boger et al., 2014). Metamorphism has been interpreted as the result of continental collision following closure of the Mozambique Ocean ("East African Orogeny" between India and east Africa) and/or the Mawson Ocean ("Kuunga Orogeny" between India–East Africa and Antarctica: Boger et al., 2015; Collins & Windley, 2002; Meert & Lieberman, 2008; Tucker et al., 2014). The metamorphic and magmatic history of the Anosyen domain is presented in more detail below.

2.1 | Metamorphism of the Anosyen sedimentary rocks

Metamorphic U–Pb zircon and monazite dates from gneisses in the Anosyen Domain are 590–500 Ma with a mode at 540 Ma (Boger et al., 2014; GAF-BGR, 2008; Giese, Berger, Schreurs, & Gnos, 2011; Horton et al., 2016; Jöns & Schenk, 2011; Martelat, Lardeaux, Nicollet, & Rakotondrazafy, 2000; Tucker, Roig, Macey, et al., 2011). These metamorphic dates are nearly identical to the dates from the granulites of southernmost India (Blereau et al., 2016; Clark et al., 2015; Johnson, Clark, Taylor, Santosh, & Collins, 2015; Taylor et al., 2014), interpreted to have been contiguous with southern Madagascar at the time. Horton et al. (2016) have also reported dates as old as 610 Ma in and near the Beraketa shear zone along the western margin of the domain, but the significance of these dates is unclear; dates older than 590 Ma within the domain are limited to a single SHRIMP zircon analysis in each of two samples described by Jöns and Schenk (2011), and two LA-ICP-MS zircon analyses from another sample described by Horton et al. (2016). A single Sm–Nd garnet–zircon–monazite–whole-rock isochron date of 588 ± 13 Ma (MSWD = 0.11) was reported for an Al-spinel–quartz leucogneiss collected near Tôlanaro (Paquette, Nédélec, Moine, & Rakotondrazafy, 1994). Martelat et al. (2000) conducted a targeted U/Th–Pb microprobe monazite dating campaign of rocks from within a variety of structural settings across south Madagascar. A regional, flat-lying "D1" granulite facies fabric was inferred to have developed between 590 and 530 Ma and been locally

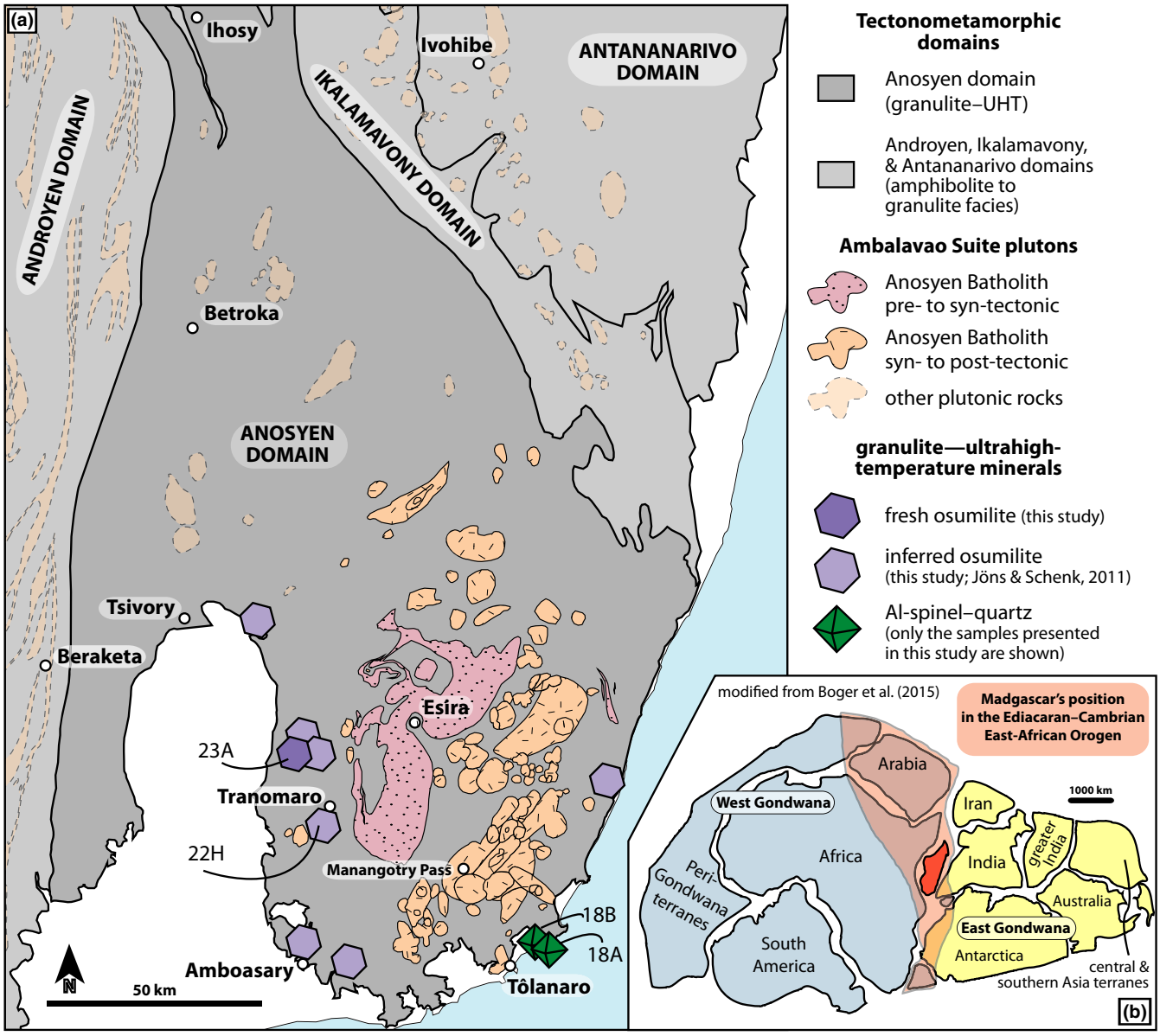

FIGURE 1 (a) Simplified geological map of the Anosyen domain in southeast Madagascar (modified from GAF-BGR, 2008). (b) The position of Madagascar during Gondwana assembly (modified from Boger et al., 2015)

overprinted by subvertical "D2" transpressional shear zones (still within the granulite facies) until sometime between 530 and 510 Ma. Martelat et al. interpreted D1 and D2 to represent a "whole progressive deformation event," rather than discrete periods of deformation. The timing of retrograde metamorphism and cooling is constrained by 550–520 Ma leucosomes and pegmatite dykes interpreted to represent partial melt crystallization (Collins, Kinny, & Razakamanana, 2012; Jöns & Schenk, 2011; Paquette et al., 1994; Tucker, Roig, Macey, et al., 2011), 537 ± 14 Ma monazite that co-crystallized with high-F apatite and biotite in metre-scale veins at 750–800°C at Manangotry Pass (Montel et al., 2018), a 453 ± 6 Ma Ar/Ar biotite date from Manangotry Pass (Montel et al., 2018) and Ar/Ar (480 ± 2 Ma) and Rb/Sr (492 ± 10, 491 ± 10 Ma) phlogopite dates from metre-scale carbonatite bodies near Beraketa (Martelat, Randrianasolo, Schulmann, Lardeaux, & Devidal, 2014).

Previous investigations indicate that the Anosyen metasedimentary rocks were metamorphosed between 0.4 and 1.1 GPa, with most studies suggesting ~0.6 GPa. Peak temperatures were >900°C in the southern portion of the domain (Tranomaro–Tôlanaro area, Figure 1) and colder in the north by 50–100°C (near and north of Ihosy, Figure 1: individual studies are outlined below). Most of the previous thermobarometric constraints are from the northern portion of the domain (near Ihosy) and along its western margin (the Beraketa shear zone), due to ease of access. The most

detailed thermobarometry of the interior of the domain was conducted by Boger, White, and Schulte (2012), who used pseudosections of three common rock types to infer peak temperatures of 880–920°C near Tranomaro and 840°C near Ihosy. Boger et al. (2012) inferred a prograde path at 0.6–0.65, with 0.1 GPa of decompression near the peak temperature, based on inclusion relationships and preserved reaction textures among minerals.

Jöns and Schenk (2011) demonstrated the regional extent of high-grade metamorphism by reporting pseudomorphs after osumilite, sapphirine–quartz, spinel–quartz and orthopyroxene–sillimanite–quartz assemblages. They used these assemblages to infer UHTM; however, fresh osumilite was not observed, and the presence of ferric iron —inferred from magnetite and hemo-ilmenite assemblages —in the sapphirine–quartz, orthopyroxene–sillimanite–quartz, and many of the spinel–quartz rocks means that the precise thermal significance of these assemblages is unclear (Kelsey, 2008). Using experimentally calibrated thermobarometers, they interpreted peak conditions of 1,000°C/1.0 GPa, followed by decompression and cooling to 800°C/0.5 GPa. Jöns and Schenk inferred that temperatures were lower near Ihosy than near Tranomaro based on a systematic south-to-north decrease in biotite and garnet Mg# (Mg/[Mg+Fe]) in biotite–garnet–sillimanite gneisses. They also estimated peak temperatures of 900–1,000°C based on reintegrated perthite compositions and the feldspar solution model of Fuhrman and Lindsley (1988).

Horton et al. (2016) calculated minimum temperatures from Ti in quartz and Zr in rutile. If the pressure was 1 GPa (GAF-BGR, 2008; Jöns & Schenk, 2011), then T_{quartz} = 930°C and T_{rutile} = 970°C. If pressure was 0.6 GPa—the pressure reported by most studies—then, T_{quartz} = 830°C and T_{rutile} = 940°C. The Ti-in-quartz temperatures are minima, because a_{TiO2} was assumed to be unity although rutile was not present in most of the samples. The Zr-in-rutile temperatures come from the Beraketa shear zone (Figure 1a), which defines the western margin of the domain; the interior of the domain might be expected to be hotter.

Martelat et al. (2012) determined the *P–T* conditions of equilibrium of a garnet leucogneiss within the Zazafotsy shear zone near Ihosy to be 800–950°C/0.9–1.1 GPa using two-feldspar thermometry (Benisek, Dachs, & Kroll, 2010; Benisek, Kroll, & Cemič, 2004; Fuhrman & Lindsley, 1988) and garnet–sillimanite–quartz–plagioclase barometry (TWEEQ). Both pressure and temperature may have been overestimated; recalculation of their GASP pressures using the THERMOCALC solution models and end-member mineral data (for direct comparison with Boger et al., 2012) and their feldspar temperatures using the solution model of Benisek et al. (2010) (correcting for K–Na diffusion using the method of Kroll, Evangelakakis and Voll (1993) for direct comparison with our results below) returns *P–T* conditions of 0.6–0.7 GPa and 750–850°C; these values are comparable to those suggested for the area near and north of Ihosy by Boger et al. (2012) and Raith, Rakotondrazafy, and Sengupta (2008).

Raith et al. (2008) calculated metamorphic conditions of 800°C/0.6–0.7 GPa from corundum–spinel–sapphirine–anorthite–phlogopite gneisses ("sakenites") 75 km northwest of Ihosy, suggesting that the northern part of the Anosyen domain experienced lower peak temperatures, consistent with the interpretations of Boger et al. (2012) and Jöns and Schenk (2011).

Rakotonandrasana, Arima, Miyawaki, and Rambeloson (2010) calculated *P–T* conditions ranging from 880°C at 0.45 GPa to 1,060°C at 0.65 GPa for högbomite–hematite-bearing pelitic rocks within the Anosyen domain just south of Ihosy using pseudosections and WinTWQ. They interpreted that the rocks experienced a component of decompression near peak temperature based on coronal relationships suggesting the reactions spinel+quartz→cordierite, and garnet+sillimanite→cordierite+spinel, but did not quantify the magnitude of decompression. They neglected ferric iron in their pseudosections, an important component given the Fe^{3+}-rich oxides in their rocks.

Ackermand (1991) calculated peak *P–T* conditions of 1 GPa and 950–980°C followed by decompression and cooling to 0.6 GPa and 800°C in silica-undersaturated sapphirine–cordierite–orthopyroxene rocks within the Beraketa shear zone, using the equilibria enstatite+sillimanite=sapphirine+cordierite, enstatite+sapphirine=cordierite+spinel, and the Al content of enstatite. They also reported metamorphic conditions of 750–950°C/0.5–0.6 GPa in metapelites near Ihosy and pressures of 0.45–0.55 GPa (no reported temperature) in garnet–cordierite–spinel gneisses near Tôlanaro.

Nicollet (1985) reported temperatures >700°C at 0.5–0.55 GPa in metapelites near Ihosy using garnet–biotite and garnet–sillimanite–cordierite–quartz equilibria. Rakotondrazafy, Moine, and Cuney (1996) recognized near-pure meionite in hibonite-bearing calcsilicate rocks near Tranomaro, implying temperatures >850°C. They also reported isochores of CO_2 fluid inclusions in corundum indicating *P–T* conditions of entrapment at 850°C/0.5 GPa. Inclusions in hibonite and anorthite indicate *P–T* conditions of entrapment at 800°C/0.35 GPa.

2.2 | Magmatism within the Anosyen domain

The Anosyen domain contains two groups of plutonic rocks: the voluminous Anosyen Batholith (Figure 1; Paquette et al., 1994; part of the broader Ambalavao Suite in GAF-BGR, 2008) and dykes, pegmatites, leucosomes and small plutons interpreted to be the result of small-volume,

partial melt crystallization during cooling. Dates for dykes, pegmatites, leucosomes and small plutons have been reported between 550 and 520 Ma (Collins et al., 2012; Jöns & Schenk, 2011; Paquette et al., 1994; Tucker, Roig, Delor, et al., 2011).

The Anosyen Batholith (Figure 1) contains "syn-" to "post-tectonic" plutons of orthopyroxene granite to syenite, garnet (±spinel) granite to syenite, quartz monzonite and one pluton of gabbro (GAF-BGR, 2008). It comprises 30–50% of the basement exposed in the southeastern part of the Anosyen domain (GAF-BGR, 2008). GAF-BGR (2008) divided the batholith into a single, large "early" pluton and many smaller "late" plutons based on whether the plutons were discordant to the granulite facies foliation ("D1" loosely constrained between 590 and 530 Ma; Martelat et al. (2000).

Eight published U–Pb zircon and monazite dates for plutons in the Anosyen batholith range from 570 to 520 Ma. GAF-BGR (2008) dated a concordant pluton at 573 ± 12 Ma and a discordant pluton at 521 ± 12 Ma (weighted mean SHRIMP $^{207}Pb/^{206}Pb$ date of youngest analyses; $^{206}Pb/^{238}U$ dates for concordant analyses range from 560 to 515 Ma) and considered these dates as representative of the "early" and "late" plutons in the batholith. Paquette et al. (1994) reported ID-TIMS U–Pb zircon intercept dates of 572 ± 14 Ma for the largest concordant body and 570 ± 3 Ma for each of two discordant orthopyroxene granites, suggesting both generations of plutons were emplaced at nearly the same time. These dates are upper intercepts of discordia that project through the origin in Wetherill concordia diagrams, consistent with Pb loss from portions of zircon grains that had experienced radiation damage: a common characteristic of U–Pb zircon data prior to the development of "chemical-abrasion" treatment (Mattinson, 2005). Sm–Nd isochrons from the same rocks agree with the U–Pb zircon intercept dates: 565 ± 7 and 555 ± 24 Ma for the concordant and discordant bodies, respectively. Paquette et al. also collected zircon Pb-evaporation dates, which were generally younger (560–530 Ma), and were considered minimum emplacement dates for the orthopyroxene granites (their discussion section). Martelat et al. (2000) reported U/Th–Pb monazite EPMA dates of 558 ± 12, 536 ± 7 and 523 ± 8 Ma from orthopyroxene granites; the two younger dates were obtained from bodies within "D2" shear zones.

3 | OSUMILITE AND Al-SPINEL–QUARTZ GNEISSES OF SOUTHERN MADAGASCAR

The samples in this study come from a 100 × 100 km area of the Anosyen domain, southeastern Madagascar, containing the Anosyen Batholith and the cities of Tranomaro, Tôlanaro, Amboasary and Esira (Figure 1). Although the study area is large, pressure estimates from within the same area (0.5–0.65 GPa: Ackermand et al., 1989; Boger et al., 2012; Rakotondrazafy et al., 1996: Section 2.1) suggest that all of the gneisses formed at nearly the same depth and record the same tectonic and thermal history. Coordinates of the sample localities used for thermobarometry and geochronology are provided in Table S2.

3.1 | Osumilite gneisses

We report the first observation of osumilite in Madagascar from sample 23A (Figure 2a). The presence of osumilite had been inferred (Jöns & Schenk, 2011) from the presence of cordierite–K-feldspar–quartz±orthopyroxene±biotite symplectites (Figure 2a–c). In most samples, these symplectites occur as near-equant 0.5–2 mm pseudomorphs within the matrix (Figure 2c) and as coronae that mantle other phases; the latter texture has been interpreted to reflect osumilite breakdown in the presence of partial melt (Korhonen, Brown, Clark, & Bhattacharya, 2013) and is consistent with the absence of orthopyroxene in most of the symplectites (Figure 2c; figure 7 in Korhonen et al., 2013). Similar symplectites have been observed in the "Bakika Formation" by Boger et al. (2012), although those authors did not interpret them to be the result of osumilite breakdown, because osumilite was not calculated to be stable in a pseudosection of that rock. Rocks with osumilite or pseudomorphs after osumilite have only been found adjacent to the Anosyen Batholith (Figure 1; Jöns & Schenk, 2011; this study). Unlike most osumilite-bearing rocks worldwide, the osumilite-bearing rocks of Madagascar do not contain orthopyroxene, except in some of the symplectites after osumilite. Two samples were chosen for pseudosection modelling and are described in more detail in the following paragraphs. Details of how the pseudosections were constructed are presented in Section 4.2.

Sample 22H contains quartz, alkali-feldspar, plagioclase, Al-spinel (with magnetite exsolution, but magnetite does not occur as separate grains; 0–0.01 atoms per formula unit each of Zn, Cr and Mn; Table S2), ilmenite, cordierite, biotite and garnet. Silicate phases are typically 200–500 μm in diameter except in cordierite–K-feldspar–quartz symplectites after osumilite (Figure 2c) and coronae (Figure 2c–g); spinel and ilmenite are typically 50–100 μm in diameter. Cordierite most commonly occurs as coronae around spinel, ilmenite, garnet, and less commonly, sillimanite. Equant cordierite also occurs in association with feldspar and quartz in the matrix. Plagioclase occurs as equant grains in the matrix and in worm-like intergrowths with quartz or alkali-feldspar; the latter are interpreted to be the result of melt crystallization. Alkali-feldspar contains exsolution lamellae of plagioclase, but plagioclase does not contain exsolution lamellae of alkali-feldspar. Biotite most

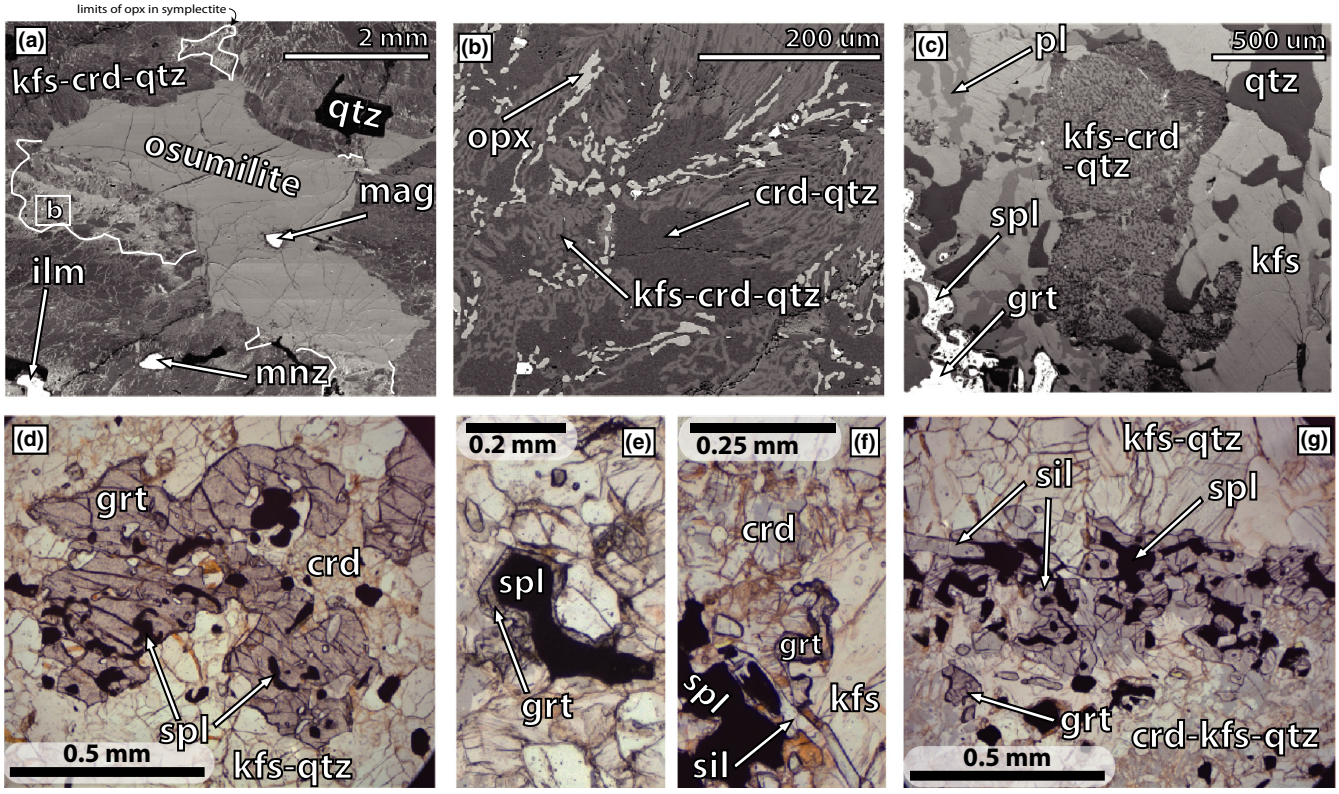

FIGURE 2 Microtextures of osumilite gneisses 23A and 22H. Mineral abbreviations after Kretz (1983). (a) Back-scattered electron (BSE) image of fresh osumilite with a magnetite inclusion, surrounded by a symplectite of K-feldspar–cordierite–quartz–orthopyroxene from sample 23A. Orthopyroxene only occurs in four restricted areas immediately adjacent to the osumilite grain. (b) Higher magnification BSE image of the symplectite in (a). (c) BSE image of K-feldspar–cordierite–quartz symplectite interpreted to be a pseudomorph after osumilite in sample 22H. (d) Optical photomicrograph of xenoblastic garnet interpreted to have grown at the expense of spinel in sample 22H. (e) Corona of garnet around spinel in sample 22H. (f) Partial corona of garnet around cordierite in sample 22H. (g) Coronae of sillimanite around spinel in sample 22H, interpreted to reflect sillimanite growth at the expense of spinel during cooling

commonly occurs rimming other mafic phases or as xenoblastic grains in the matrix. Garnet occurs as up to 1 mm xenoblastic grains with ubiquitous inclusions of Al-spinel (no Zn or Cr), quartz and sillimanite (Figure 2d), as 100–200 μm coronae around Al-spinel (Figure 2e), and, in one location, as a partial corona around cordierite (Figure 2f). Outside garnet, sillimanite occurs as a matrix phase and as coronae around Al-spinel (Figure 2g).

Sample 23A is the only sample in which fresh osumilite was observed. Fresh osumilite occurs at the centre of a 1.5 cm-wide fine-grained symplectite of alkali-feldspar, cordierite, quartz, orthopyroxene and magnetite (Figure 2a,b). Orthopyroxene was only found in the symplectite immediately adjacent to the fresh osumilite; even adjacent to the osumilite, its presence is spatially restricted (Figure 2a). Orthopyroxene is not present near the spinel–quartz–sillimanite–feldspar matrix. The symplectite minerals are elongate perpendicular to the boundary of the fresh osumilite; abrupt changes in the orientations and modal proportions of minerals within the symplectite are inferred to be former osumilite grain boundaries. The fresh osumilite contains a single inclusion of magnetite (Figure 2a). Quartz, alkali-feldspar, magnetite, ilmenite and monazite occur as inclusions within the fine-grained symplectite near the fresh osumilite; these phases are interpreted to have been former inclusions in osumilite. Biotite and coarser grained cordierite occur as xenoblastic grains and coronae around spinel, magnetite, and ilmenite that extend into the symplectite near its margins. Large zircon (up to 200 μm) and a single monazite are associated with one biotite corona around a composite magnetite–ilmenite grain (Section 5.2, below).

3.2 | Al-spinel–quartz gneisses

The gneisses along the southeast coast of Madagascar (south and east of the Anosyen Batholith; Figure 1) consist mainly of leucogneiss dominated by a single ternary feldspar (now mesoperthite), quartz, and garnet with minor Al-spinel, ilmenite and sillimanite (Figures 3 and 4). Spinel occurs mainly in intergrowths with quartz adjacent to garnet (Figure 3a,b), but also as isolated grains in the matrix. Magnetite exsolution is absent or makes up <1 vol.% of the spinel in all samples of this rock type. Spinel is commonly separated from quartz by 20–100 μm coronae of

garnet, sillimanite, garnet–sillimanite or plagioclase (Figure 3b–d). Cordierite coronae around garnet and spinel are present in some samples, but not sample 18A used for pseudosection modelling. Biotite is a local retrograde phase around spinel and garnet. Plagioclase occurs as films along mesoperthite grain boundaries (Figure 4) and in intergrowths with quartz, suggesting growth from the exsolution of ternary feldspar and from melt crystallization. Garnet contains inclusions of alkali-feldspar and quartz.

4 | THERMOBAROMETRY

4.1 | Feldspar thermometry

Minimum temperatures of metamorphism were calculated from reintegrated mesoperthite compositions and plagioclase films along mesoperthite grain boundaries in two hercynite–quartz gneisses (samples 18A and 18B: Figure 4). The solution model and Na–K exchange correction recommended by Benisek et al. (2010) were used. The pressure used in the calculations was 0.6 GPa. Analytical uncertainties on feldspar compositions were 0.5, 0.9, 0.5, 5.0, 0.5, 7.6 and 0.5% for X_{ab}^{pl}, X_{an}^{pl}, X_{ab}^{af}, X_{an}^{af}, X_{san}^{af}, X_{san}^{pl} and X_{san}^{af}, respectively (EPMA analyses in Tables S2 and S3). Calculations were done 2,000 times by Monte-Carlo simulation from plagioclase–reintegrated mesoperthite compositional pairs. The temperatures and uncertainties reported below reflect the median and 95% confidence interval of the Monte-Carlo simulation. Calculations in which the standard deviation of T_{ab}, T_{an} and T_{san} never decreased below 10°C during the Na-K exchange correction were excluded (see Benisek et al., 2010 for explanation of T_{ab}, T_{an} and T_{san}).

The four perthites from sample 18A returned temperatures of 882 +45/−107, 943 +29/−48, 899 ± 34 and 913 ± 13°C. The four perthites from sample 18B returned temperatures of 919 +17/−30, 927 +28/−48, 932 ± 23 and 922 +25/−31°C. All calculated temperatures agree between 910 and 930°C; this is a minimum temperature estimate for these rocks. Jöns and Schenk (2011) also presented ternary feldspar thermometry temperatures: 900–1,000°C using the solution model of Fuhrman and Lindsley (1988). Their slightly higher temperatures are the result of lower miscibility in the Fuhrman and Lindsley (1988) solution model, compared to the Benisek et al. (2010) model. For a discussion of the different feldspar solution models, see Benisek et al. (2010).

4.2 | Phase-equilibria modelling

Pseudosections for two osumilite gneisses and one Al-spinel–quartz gneiss were constructed (Figures 5 and 6) using bulk compositions calculated from mineral modes in thin section, mineral molar volumes and mineral compositions measured by EPMA (Table S4). Oxide components used in the calculations were Na_2O, CaO, K_2O, FeO, Fe_2O_3, MgO, MnO, Al_2O_3, SiO_2, TiO_2 and H_2O. Calculations were made using the gridded minimization algorithm of Perple_X 6.7.8 (Connolly, 2009). Diagrams were constructed using the mineral end-member thermodynamic database of Holland and Powell (2011). The ternary feldspar solution model used is from Benisek et al. (2010) to facilitate direct comparison with feldspar temperatures (Section 4.1). The osumilite solution model used is that of Holland, Babu, and Waters (1996). Garnet, cordierite,

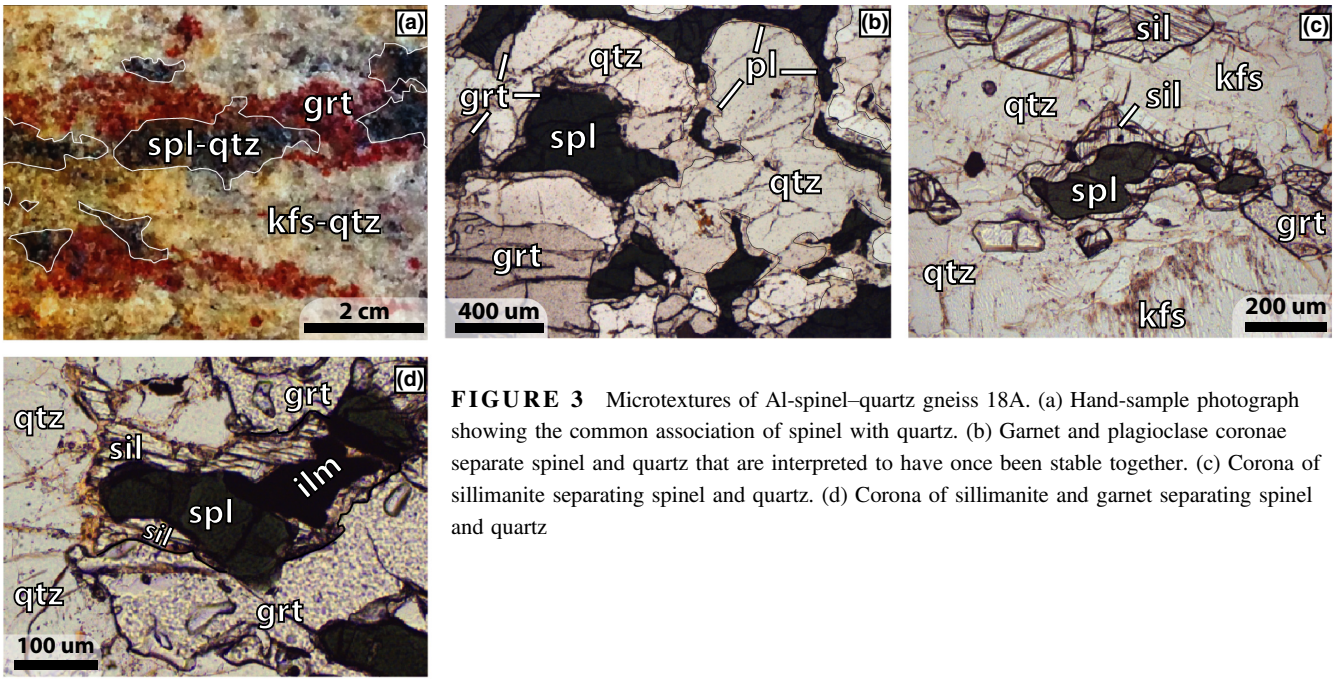

FIGURE 3 Microtextures of Al-spinel–quartz gneiss 18A. (a) Hand-sample photograph showing the common association of spinel with quartz. (b) Garnet and plagioclase coronae separate spinel and quartz that are interpreted to have once been stable together. (c) Corona of sillimanite separating spinel and quartz. (d) Corona of sillimanite and garnet separating spinel and quartz

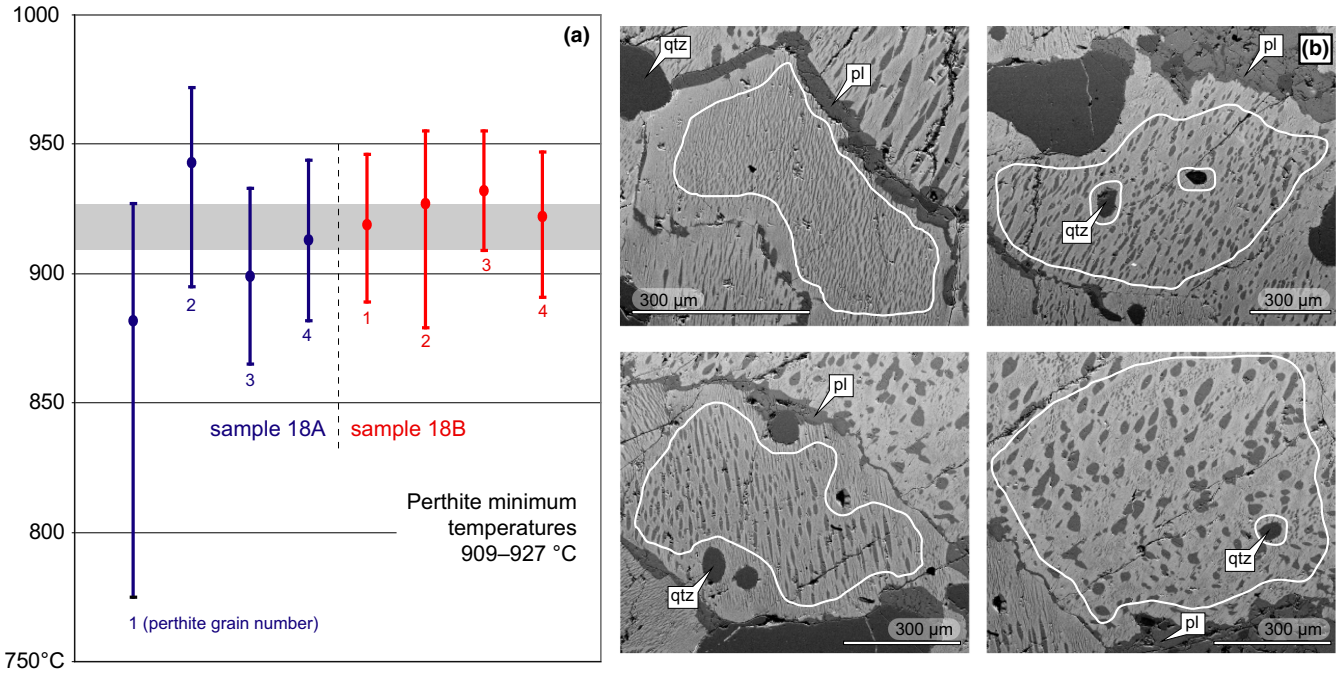

FIGURE 4 (a) Mesoperthite and adjacent, grain-boundary plagioclase—interpreted to have formed during exsolution—record a minimum metamorphic temperature of 910–930°C. (b) Mesoperthite grains used for thermometry in sample 18A. Shapes show the areas of perthite reintegrated for thermometry. Mineral abbreviations after Kretz (1983)

silicate melt, biotite and orthopyroxene are from White, Powell, Holland, Johnson, and Green (2014) and White, Powell, and Johnson (2014); ilmenite is from White, Powell, Holland, and Worley (2000) with $MgTiO_3$ added as described by White, Powell, Holland, et al. (2014) and $MnTiO_3$ added as described by White, Powell, and Johnson (2014); spinel is from White, Powell, and Clarke (2002).

4.2.1 | Elemental components not included in the osumilite solution model

EPMA measurements of osumilite in sample 23A indicate 0.01 atoms of Ti, 0.04 atoms of Mn, 0.06 atoms of Ca and 0.01 atoms of Na per formula unit (30 oxygen; Table S2). The osumilite model of Holland et al. (1996) does not include Ti, Na, Ca, Mn, Fe^{3+} or vacancies. The effects these components have on osumilite stability are not known and must be considered when interpreting the pseudosections of this manuscript. Experiments by Das, Dasgupta, and Miura (2001) in K_2O–FeO–Fe_2O_3–MgO–Al_2O_3–SiO_2–H_2O suggest osumilite stability at high fO_2 is restricted to > 850°C/<0.85 GPa—similar to its stability at low fO_2 conditions (Carrington & Harley, 1995)—but whether Fe^{3+} is actually incorporated into osumilite in significant amounts remains unclear (see discussion by Das et al., 2001). The osumilite of sample 23A, in this study, has an average cation total of 18.07 for 30 oxygen; 0.4% higher than the expected 18 cations for the simplified osumilite solid solution used in the Holland et al. (1996) solution model. A higher than expected cation total may indicate that molecular weight was underestimated in the processing of EPMA measurements, possibly related to the additional oxygen bonded to ferric relative to ferrous iron. This argument, however, hinges on the assumption that osumilite should have exactly 18 cations per 30 oxygen. For natural osumilite, reported cation totals are typically slightly less than 18 (Armbruster & Oberhaesnsli, 1988; Berg & Wheeler, 1976; Chinner & Dixon, 1973; Olsen & Bunch, 1970); a notable exception is the osumilite reported by Arima and Gower (1991). Even the osumilite from the hematite–magnetite buffered experiments of Das et al. (2001), has cation totals slightly less than 18; suggesting that cation totals are not a reliable method for estimating ferric iron content. Furthermore, most of the "excess" cations calculated for osumilite in sample 23A can be accounted for by the excess alkalis. The sum of Na, K and Ca is, on average, 1.04: the maximum occupancy of the 12-fold coordinated A site is unity. The excess alkali metals may be indicative of partial occupancy of an additional site—the B site—that has been suggested for other osumilite group minerals yagiite (Bunch & Fuchs, 1969), roederrite (Fuchs, Frondel, & Klein, 1966; Olsen, 1967) and merrihueite (Dodd, Schmus, & Marvin, 1965; see Berg & Wheeler, 1976). Finally, wt% totals for osumilite in this study are 100.4 on average, suggesting that total molecular weight has been slightly overestimated, not underestimated. Despite the presence of hematite–ilmenite and spinel–magnetite solid solutions in sample 23A, the extent to which Fe^{3+} is accommodated in osumilite remains unclear.

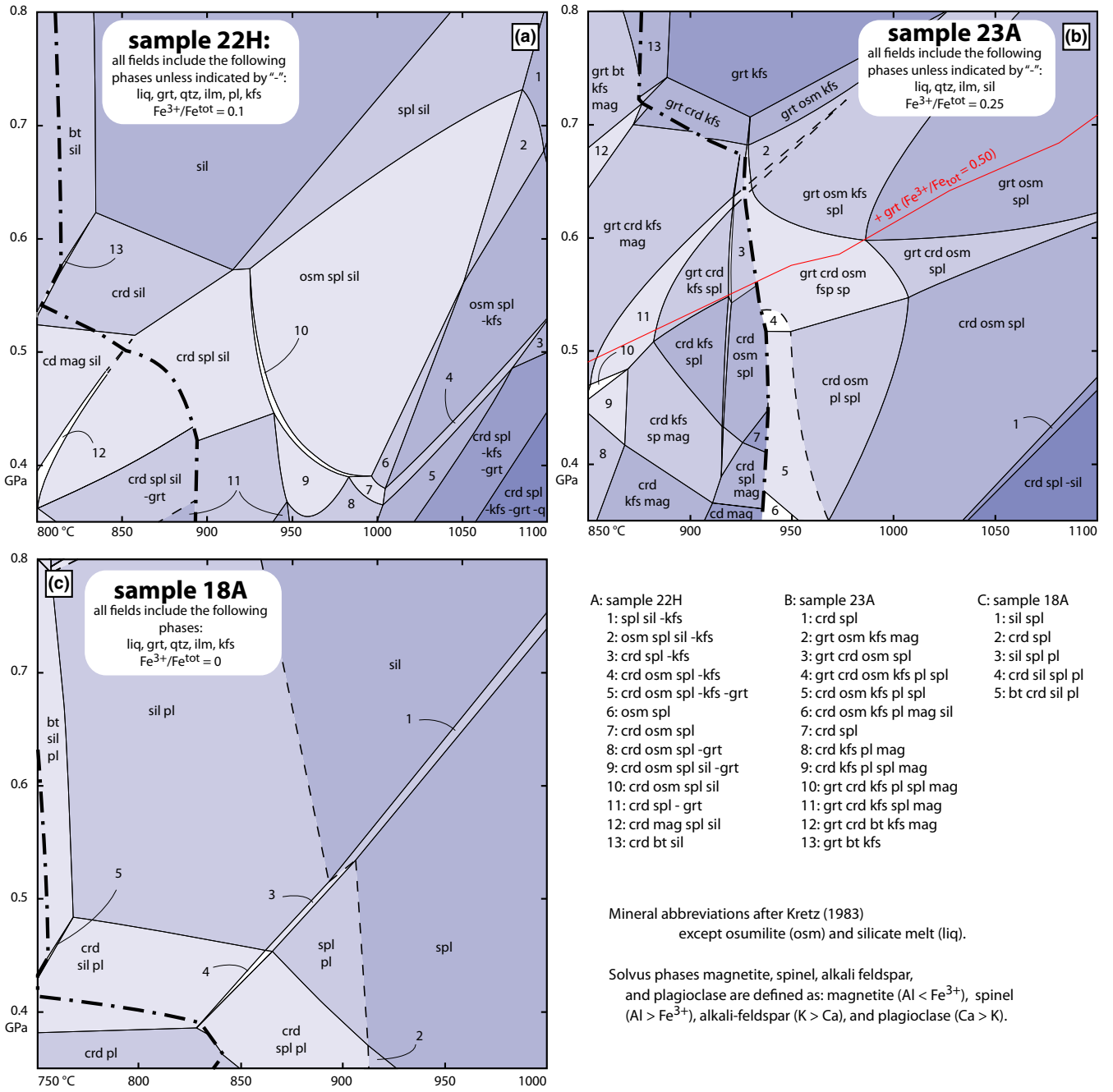

A: sample 22H
1: spl sil -kfs
2: osm spl sil -kfs
3: crd spl -kfs
4: crd osm spl -kfs
5: crd osm spl -kfs -grt
6: osm spl
7: crd osm spl
8: crd osm spl -grt
9: crd osm spl sil -grt
10: crd osm spl sil
11: crd spl - grt
12: crd mag spl sil
13: crd bt sil

B: sample 23A
1: crd spl
2: grt osm kfs mag
3: grt crd osm spl
4: grt crd osm kfs pl spl
5: crd osm kfs pl spl
6: crd osm kfs pl mag sil
7: crd spl
8: crd kfs pl mag
9: crd kfs pl spl mag
10: grt crd kfs pl spl mag
11: grt crd kfs spl mag
12: grt crd bt kfs mag
13: grt bt kfs

C: sample 18A
1: sil spl
2: crd spl
3: sil spl pl
4: crd sil spl pl
5: bt crd sil pl

Mineral abbreviations after Kretz (1983) except osumilite (osm) and silicate melt (liq).

Solvus phases magnetite, spinel, alkali feldspar, and plagioclase are defined as: magnetite ($Al < Fe^{3+}$), spinel ($Al > Fe^{3+}$), alkali-feldspar ($K > Ca$), and plagioclase ($Ca > K$).

FIGURE 5 Pseudosections of (a) osumilite-garnet gneiss 22H, (b) osumilite gneiss 23A, and (c) Al-spinel–quartz gneiss 18A. Bold, dash-dot lines are the residual solidi: the water content at temperatures higher than these lines was set such that the interpreted peak assemblages did not contain more than 10 vol.% melt. At temperatures below this line, additional H_2O was added to the calculations to stabilize melt, thereby providing a better model of melt-saturated phase relationships during prograde metamorphism (see text for more details and discussion of melt-reintegration methods). The positions of dashed phase boundaries were poorly constrained by the calculation (typically the spinel and feldspar solvi). Darker shading indicates higher variance mineral assemblages

4.2.2 | Elemental components not included in the spinel solution model

The spinel–magnetite model of White et al. (2002) does not include Mn, Cr or Zn. In sample 22H, Mn and Cr are 0.00–0.01 atoms per formula unit (apfu: four oxygen); in sample 23A, Mn was 0.01–0.02 apfu; and in sample 18A1 Zn was 0.01 apfu (Table S2). The effect of Zn on Al–spinel stability was studied experimentally by Nichols, Berry, and Green (1992). While Zn can greatly expand spinel's stability to lower temperatures and higher pressures, the small amount of $ZnAl_2O_4$ in the spinel of this study is negligible considering the geological and numerical uncertainties in thermobarometry and phase equilibria; 0–0.01 apfu

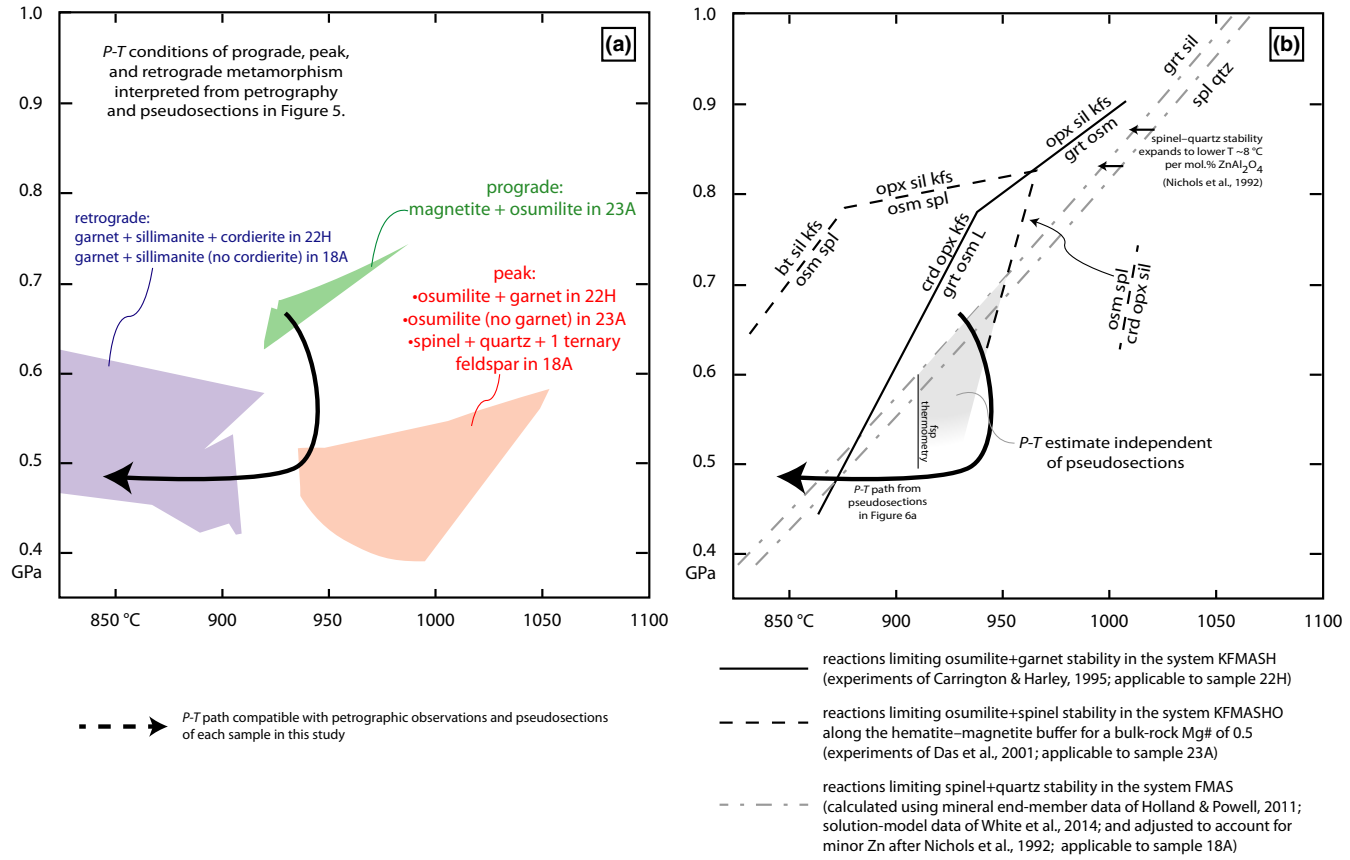

FIGURE 6 Interpreted pressures and temperatures of metamorphism for the samples in this study. (a) The stability fields of prograde, peak and retrograde mineral assemblages from pseudosections in Figure 5. (b) Independent estimates for the *P–T* conditions of the samples in this study. Osumilite in sample 23A contains Na, Ca, Ti, Mn and possibly Fe^{3+}, none of which are accounted for in the osumilite solution model used in Figures 5 and 6a. Independent estimates for osumilite stability are provided by the experiments of Das et al. (2001; high fO_2) and Carrington and Harley (1995; low fO_2). Spinel in sample 18A contains <1 mol.% $ZnAl_2O_4$, which is not accounted for in the spinel solution model used in Figures 5 and 6a. The effect of Zn on spinel stability was evaluated by Nichols et al. (1992); for 1 mol.% $ZnAl_2O_4$, the stability of spinel with quartz expands ~8°C down temperature. Feldspar thermometry provides an additional, independent *P–T* constraint. Estimates of peak temperature from these methods are only slightly lower than estimates from pseudosections

corresponds to <8°C down-temperature shift in spinel–quartz stability. The effect of Mn and Cr on spinel stability is not known, but likely to be similarly negligible considering their low concentrations. Together, the spinel–quartz stability calculations and feldspar thermometry provide independent *P–T* estimates from those constrained by the osumilite stability calculations.

4.2.3 | Elemental components not included in the biotite solution model

Fluorine can increase the stability of biotite to higher temperature (Dooley & Patiño Douce, 1996; Finch & Tomkins, 2017; Motoyoshi & Hensen, 2001), but is not included in the solution model of White, Powell, Holland, et al. (2014). In all modelled samples, biotite occurs as coronae around other mafic phases or as xenoblastic grains in the matrix and is interpreted to be exclusively retrograde in these samples; the *P–T* interpretations of this study do not rely on reactions involving biotite.

4.2.4 | Samples chosen for pseudosections

Two samples of osumilite gneiss were modelled. (1) Sample 22H was chosen because of its relatively low ferric iron content compared to the other osumilite-bearing rocks; there is no magnetite other than exsolution lamellae in spinel and there is no hematite exsolution in ilmenite. (2) Sample 23A was chosen because it is the only sample with fresh osumilite. The ferric iron contents of samples 22H and 23A were estimated from the observed modes and compositions of mafic phases. These values were then adjusted iteratively during the construction of the pseudosections until the approximate measured oxide compositions were reproduced at the inferred peak *P–T* conditions. For 22H, this resulted in $Fe^{3+}/Fe^{total} = 0.1$; for 23A, 0.25. To test the sensitivity of

the outputs to different ferric iron contents, pseudosections were calculated at half and twice the values described above; the main effects were changes in the lower temperature stability limit of Al-spinel and reactions involving ilmenite outside the *P–T* conditions relevant to the rock. The key relationships of osumilite±garnet were affected by less than 0.1 GPa and 25°C (Figure 5b). As discussed above, and again below, the results of osumilite-bearing pseudosections are limited by the lack of Fe^{3+}, Mn, Ca, Na and Ti in the osumilite solution model.

Of the hercynite–quartz gneisses, sample 18A was chosen for pseudosection modelling because it lacks retrograde cordierite and therefore provides a low-*P* constraint on the retrograde *P–T* path. Furthermore, the spinel contains no magnetite exsolution, <1 mol.% $ZnAl_2O_4$, and no measurable Cr, indicating that its stability should be well described by the spinel solution model of White et al. (2000). Ilmenite is end-member $FeTiO_3$, corroborating the lack of ferric iron in the rock.

The H_2O content in all calculations was set such that the silicate melt was ~10 vol.% at the inferred peak *P–T* conditions; this was ~0.5 mol.% H_2O for all rocks. Due to these low H_2O contents, the lower temperature mineral assemblages in the initial pseudosection calculations were melt absent. To better illustrate the potential prograde phase equilibria (prior to melt extraction), the portions of the diagrams at lower temperature were recalculated both by reintegrating melt (as described by Korhonen et al., 2013) and by simply increasing the bulk-rock water content until the entire diagrams became melt-saturated. The results of both methods were nearly identical, because the two most abundant components of the reintegrated silicate melt were, by far, H_2O and SiO_2; the additional SiO_2 has no effect on the phase equilibria, because the modelled assemblages are already saturated in SiO_2. This is consistent with the findings of Bartoli (2017) who tested different methods of melt reintegration and found that the stability limits of phases were similar in all calculations. The phase equilibria at temperatures lower than the low-H_2O solidi in Figure 5 (bold dash-dot lines; referred to as residual solidi elsewhere) were obtained by increasing the bulk-rock water content, as this was both a simpler and more objective calculation. The amount of water required to saturate the full diagrams with melt was 2–3 mol.%. Although these calculations illustrate potential prograde phase relationships, no detailed inferences about the low-temperature *P–T* path of the rocks are made in this study due to a lack of definitively prograde mineral relationships.

4.3 | Pressure–temperature path

Pressure–temperature path inferred from pseudosections: The peak temperature reached by sample 18A (Al-spinel–quartz gneiss) is constrained by the stability of one ternary feldspar+spinel: >910°C (Figure 5c). The peak *P–T* conditions reached by sample 22H (osumilite–garnet gneiss) are constrained by the stability of osumilite–garnet–spinel: 925–1,050°C/0.4–0.7 GPa (Figure 5a). The peak *P–T* conditions reached by sample 23A (fresh osumilite gneiss) are constrained by the stability of osumilite without garnet: >940°C/<0.6 GPa (Figure 5c). The inferred peak temperature mineral assemblages in pseudosections of all samples overlap in the range of 940–1,050°C/0.4–0.6 GPa (Figure 6a).

The dominant coronal relationships preserved in the osumilite and Al-spinel–quartz gneisses consist of garnet and sillimanite mantling Al-spinel and are interpreted to be indicative of the FMAS reactions spinel+quartz→garnet+sillimanite during cooling (and related reactions in more chemically complex systems; Figures 2 and 3). The ubiquity of Al-spinel, sillimanite and quartz inclusions in garnet from sample 22H (Figure 2) are also interpreted to reflect retrograde garnet growth by this reaction. Similar microtextures were identified in granulites from the Musgrave Block of central Australia by White et al. (2002) and interpreted to be the result of the same reaction (alternatively, Boger et al., 2012; interpreted similar garnet [no sillimanite] coronae around magnetite and Al-spinel to reflect garnet growth during prograde biotite breakdown; Zn in Al-spinel was invoked as a mechanism that might have stabilized Al-spinel to lower temperatures than garnet allowing garnet to grow around spinel during heating). The moderate Clapeyron slope of the reaction spinel+quartz→garnet+sillimanite (see figure 2 of White, Powell, & Holland, 2007) prohibits robust interpretation of the nature of the *P–T* path (clockwise, counterclockwise, or isobaric). However, the presence of retrograde cordierite in sample 22H, but not 18A, requires near-isobaric cooling through the granulite facies at ~0.45–0.6 GPa (Figure 6b). Magnetite inclusions in osumilite from sample 23A are compatible with either a clockwise (Figure 6a) or counterclockwise *P–T* path, but a clockwise *P–T* path is more consistent with the observations of Boger et al. (2012) and Jöns and Schenk (2011); uncertainty in the prograde path is discussed in more detail below.

Comparison with other *P–T* estimates: The stability limits of osumilite must be interpreted with caution due to the absence of minor components in the solution model. Independent estimates for the *P–T* conditions of metamorphism are provided by the stability limit of spinel–quartz in sample 18A (garnet+sillimanite=spinel+quartz in the system FeO–MgO–Al_2O_3–SiO_2 adjusted for minor Zn after Nichols et al., 1992), feldspar thermometry (Section 4.1), the experimental stability limits of osumilite–garnet in low fO_2 rocks (Carrington & Harley, 1995), and the experimental stability limits of

osumilite in high fO_2 (Das et al., 2001). Together, these independent *P–T* estimates suggest metamorphism at 910–950°C/<0.65 GPa, although the upper temperature limit is poorly constrained by extrapolation of the experiments of Das et al. (2001) to lower pressure (Figure 6b). These *P–T* estimates are not significantly different than those inferred from pseudosections of osumilite-bearing rocks above. Viewed holistically, the temperature estimates of this study agree with those of Jöns and Schenk (2011: 900–1,000°C) and the upper limit of the estimates of Boger et al. (2012: 880–920°C).

The pressures obtained in this study and Boger et al. (0.4–0.6 GPa) are lower than those obtained by Jöns and Schenk (2011; 1.0 GPa). This may be the result of different thermobarometric approaches or differences in the rocks targeted in each study. Jöns and Schenk (2011) determined peak pressures and temperatures from the intersections of experimentally calibrated thermobarometers from different rocks (e.g. intersection of Al in orthopyroxene in one rock with GASP in another rock). When using internally consistent thermobarometers from single rocks along the western margin of the domain (using the AvPT method of THERMOCALC), the calculated *P–T* conditions were 936 ± 190°C/0.83 ± 0.2 GPa (2σ), which are compatible with the *P–T* conditions reported by Boger et al. (2012) and this study. An additional limitation in comparing the *P–T* estimates from Jöns and Schenk (2011) and this study is that many (but not all) of the *P–T* estimates of Jöns and Schenk came from rocks along the western margin of the Anosyen domain and in the Androyen domain, whereas the thermobarometry in this paper comes from the central and eastern portion of the domain (Figure 1). The higher pressures estimated by Jöns and Schenk could, in part, reflect higher metamorphic pressures to the west.

Prograde metamorphism between 0.55 and 0.7 GPa was determined by Boger et al. (2012) based on the inferred co-stability of garnet, sillimanite and cordierite during prograde metamorphism within the "Bakika" and "Amparihy" formations. Alternatively, a higher-pressure prograde path (≥1 GPa) was suggested by Jöns and Schenk (2011) based on the intersections of garnet–plagioclase–orthopyroxene–quartz, garnet–sillimanite–quartz–plagioclase, and garnet–orthopyroxene (Al in orthopyroxene) equilibria from different rocks. Both studies inferred a clockwise *P–T* path based on retrograde growth of cordierite. In sample 23A of this study, fresh osumilite contains inclusions of magnetite (Figure 2a). This inclusion relationship is consistent with heating at ~0.65 GPa (as proposed by Boger et al., 2012) or during isothermal decompression at ~950°C (as proposed by Jöns & Schenk, 2011). Although the prograde path remains poorly constrained, all interpretations are compatible with a clockwise *P–T* path passing through ~900°C/0.5 GPa. In Section 5, we demonstrate that such a *P–T* path is also compatible with observed trends in monazite composition from sample 22H.

Orthopyroxene in the symplectites after osumilite in sample 23A: Orthopyroxene is present in the symplectites after osumilite in sample 23A (Figure 2a), but does not occur as a stable phase in the pseudosection of that sample (Figure 5b). Phase stability within fine-grained symplectites has been demonstrated to reflect local chemical potential gradients that develop as a result of limited and differential elemental mobility at the time of symplectite formation (Schorn & Diener, 2017; Štípská, Powell, White, & Baldwin, 2010; White, Powell, & Baldwin, 2008). This has been shown most starkly by Baldwin, Powell, White, and Štípská (2015) who documented sapphirine, corundum and spinel as spatially restricted components of symplectites after kyanite in quartz-bearing high-*P* granulites. Pseudosections constructed from whole-rock compositions showed that none of these phases were part of an equilibrium mineral assemblage at the hand-sample or thin-section scale (corundum may never be stable with quartz: Harlov & Milke, 2002); rather, the limited elemental mobility created chemical potential gradients between the kyanite and surrounding matrix resulting in heterogeneous distribution of minerals within the symplectites.

In sample 23A, orthopyroxene was only found in K-feldspar–cordierite–quartz symplectites immediately adjacent to fresh osumilite; even adjacent to the osumilite, its presence is spatially restricted (Figure 2a). Such restricted and discontinuous occurrence of orthopyroxene within the symplectites of this sample is similar to the restricted and discontinuous occurrence of spinel/sapphirine/corundum in the examples described above. We interpret orthopyroxene adjacent to osumilite to be the result of local chemical potential gradients during symplectite formation, rather than part of an equilibrium mineral assemblage at the thin-section scale. The absence of orthopyroxene from the pseudosection of this sample (Figure 5b) is consistent with this interpretation. For an additional example of chemical potential gradient-controlled mineral stability, the reader is referred to Štípská, Powell, and Racek (2014) and Štípská, Powell, Racek, and Lexa (2014). For a more general discussion on the scale of equilibrium during high-grade metamorphism, the reader is referred to Guevara and Caddick (2016).

5 | U–Pb LASER-ABLATION-SPLIT-STREAM ICP-MS MONAZITE AND ZIRCON GEOCHRONOLOGY

Monazite and zircon were dated by Laser-ablation split-stream ICP-MS (LASS). Details of these analyses are presented in Appendix S3; data are in Tables S5 and

S6. For further explanation of the method, see Kylander-Clark, Hacker, and Cottle (2013) and Kylander-Clark (2017). The reported dates in this paper are weighted means of multiple analyses. The reported uncertainties reflect the 2SE of the weighted means and should only be used to compare dates from the same mineral (monazite with monazite or zircon with zircon) within this study. For comparing zircon and monazite dates or dates from either mineral with dates from other studies, a 2% uncertainty should be used, reflecting the long-term reproducibility of homogeneous reference materials in the laser-ablation ICP-MS laboratory at the University of California, Santa Barbara.

5.1 | U/Th–Pb LASS monazite

5.1.1 | Monazite U/Th–Pb dates and their relationship to the *P–T* path

Concordia diagrams of all samples are presented in Figure 7. Discordant analyses from samples 21A, 23C, 18B and MD69 define a discordia with an upper intercept near 1,900 Ma and are coloured red; these dates correspond to the dominant peak in detrital zircon from the Anosyen domain and related metasedimentary rocks in Madagascar and south India (Boger et al., 2014; Collins et al., 2012). Analyses that are coloured red and dashed, but appear concordant in U–Pb concordia diagrams (Figure 7a–f), have discordant U–Pb–Th–Pb isotopic ratios. Dates mentioned below are U–Pb dates.

The oldest concordant analyses from all samples that are statistically indistinguishable by the MSWD criterion (Wendt & Carl, 1991) are 579 ± 5 Ma. These analyses correspond to a minor peak in the PDF of all concordant dates (Figure 7i) and are interpreted to reflect monazite neocrystallization during prograde metamorphism (450–600°C; Spear, 2010).

Large monazite grains within symplectite after osumilite in sample 23A are interpreted to have been former inclusions in osumilite (Section 3.1 and Figure 2a). All analyses from these inclusions are 561 ± 6 Ma (Figure 7h). Based on the inferred inclusion relationship, this is a maximum date for osumilite growth and for the peak temperature of metamorphism. This date coincides with emplacement ages of the older generation of plutons in the Anosyen Batholith.

Monazite with oscillatory zoning (Figure S1) located within a segregation of equant feldspar, quartz and cordierite in sample 23A is interpreted to have crystallized as the rock cooled through its solidus. Based on the residual solidus calculated for this sample (Figure 5b), the temperature at the time that this monazite grew was 930–940°C. All analyses from this monazite yield a mean date of 550 ± 6 Ma (Figure 7g). This is the oldest reported date for partial melt crystallization in the Anosyen domain (Section 2.2), and thus a minimum date for the peak temperature of metamorphism.

A majority of the monazite analyses are younger than 550 Ma (Figure 7i) and define two peaks: 535 and 522 Ma. These broad peaks correspond to dates reported for leucosome, pegmatite, small-pluton and hydrothermal crystallization during cooling of the domain (Collins et al., 2012; Jöns & Schenk, 2011; Paquette et al., 1994; Tucker, Roig, Delor, et al., 2011; Tucker, Roig, Macey, et al., 2011). This is consistent with models of monazite solubility in silicate melts: monazite is predicted to dissolve during high-grade metamorphism and precipitate during cooling and melt crystallization (Stepanov, Hermann, Rubatto, & Rapp, 2012).

5.1.2 | Monazite composition

Monazite dates from sample 22H span the entirety of the metamorphic event and display trends in composition; the petrological significance of these trends is discussed here. The compositional variables discussed are Gd/Yb and Eu/Eu* (Eu* = $[Sm \times Gd]^{0.5}$); values used in the ratios are normalized to concentrations of the elements in C.I. chondrite (McDonough & Sun, 1995). Monazite dates from each of the other samples only span a portion of the metamorphic event and many of the analyses in each of these samples are the same age within uncertainty, meaning that trends in monazite composition cannot be reliably identified; compositions of monazite in these samples are not discussed.

Gd/Yb in sample 22H decreases between 580 and 550 Ma, after which it increases (Figure 8a). This pattern can be seen in individual monazite grains (Figure 8c): low-Y (high Gd/Yb) cores were mantled/replaced by high-Y (low Gd/Yb) mantles, and then followed by low-Y rims (high Gd/Yb). Eu/Eu* exhibits the same trend (Figure 8d).

Monazite Gd/Yb and garnet growth/resorption

We interpret decreases in monazite Gd/Yb to reflect garnet breakdown, whereas increases are interpreted to reflect garnet growth (e.g. Mottram et al., 2014; Rubatto, Hermann, & Buick, 2006; Stearns et al., 2013). For sample 22H, this implies that the mode of garnet decreased at *c.* 550 Ma and subsequently increased (Figure 8a,b). This is consistent with the petrographic interpretation of retrograde garnet growth by the reaction spinel+quartz→garnet+sillimanite (Figure 2; Section 4.2.1) and with six of seven analyses from monazite inclusions in garnet having dates younger than 550 Ma (Figure 8a). These trends are compatible with metamorphism along a clockwise *P–T* path, in which the mode of garnet decreases towards high temperature and

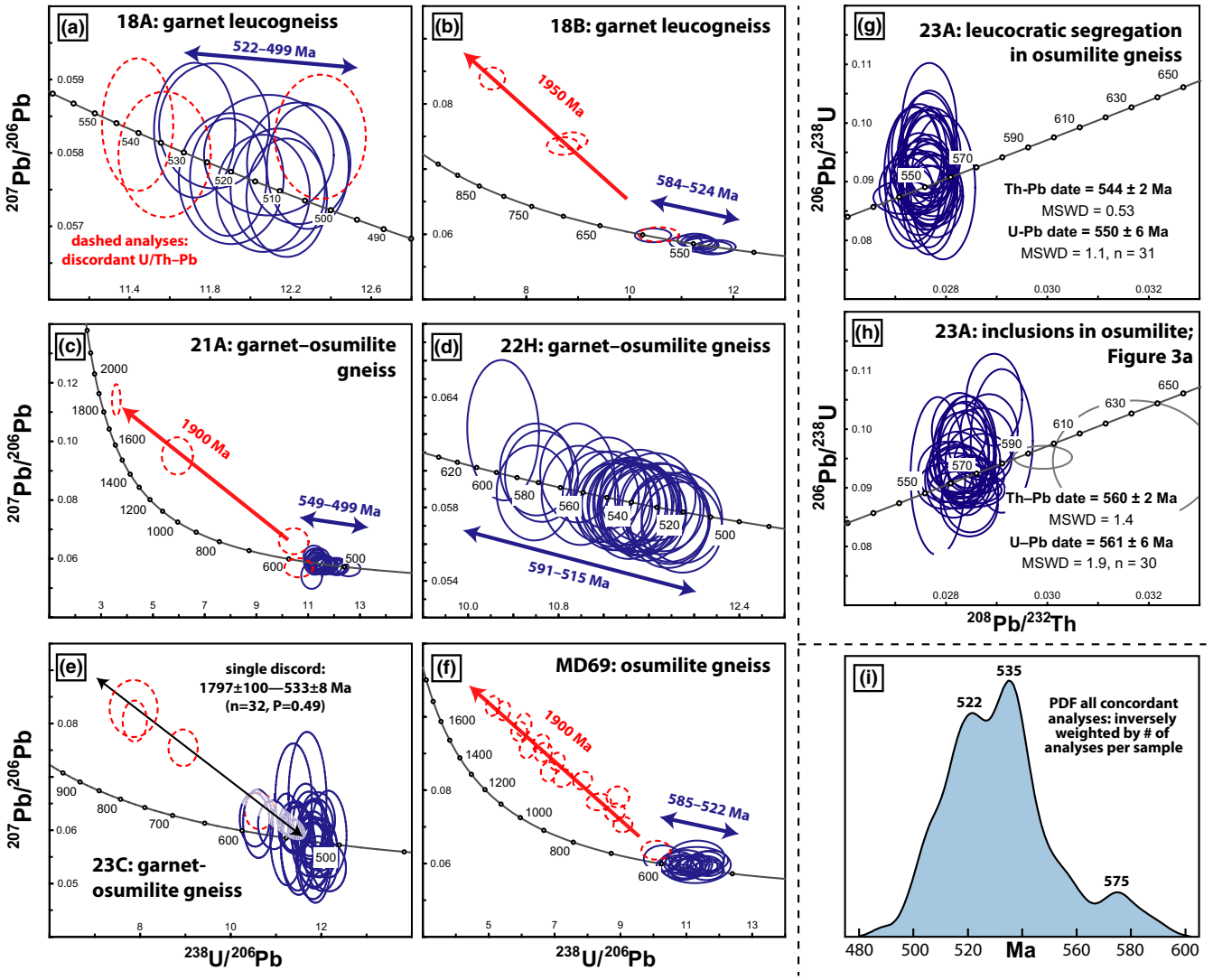

FIGURE 7 (a–f) Concordant monazite dates record 80 Ma of tectonic and thermal activity in the Anosyen domain from 580 to 500 Ma. (g–h) Monazite inclusions in osumilite and from a leucocratic segregation—interpreted to have formed during melt crystallization—at the same outcrop constrain the timing of peak metamorphism between 561 ± 6 and 550 ± 6 Ma. (i) PDF of all concordant monazite dates inversely weighted by number of analyses per sample. The oldest dates define a peak at 575 Ma—interpreted as prograde monazite neocrystallization—whereas the majority of analyses are <550 Ma and interpreted to reflect growth or recrystallization during cooling

low pressure and subsequently increases during cooling (Figure 8b).

Monazite Eu/Eu* as a record of changes in oxidation state

Changes in Eu/Eu* in monazite have been interpreted to reflect changes in the mode of feldspar (e.g. Holder, Hacker, Kylander-Clark, & Cottle, 2015; Mottram et al., 2014; Rubatto et al., 2006): increases reflect feldspar breakdown and decreases reflect feldspar growth. According to this hypothesis, Eu/Eu* in monazite should increase during partial melting within the granulite facies as feldspar breaks down, and decrease during melt crystallization as feldspar grew. This trend is opposite to that observed in sample 22H: Eu/Eu* decreases during partial melting (feldspar breakdown) and increases during melt crystallization (feldspar growth; Figure 8d,f).

Implicit, but never discussed in the model described above, is that bulk-rock Eu^{3+}/Eu^{total} is less than unity, Eu^{3+}/Eu^{total} is constant, and $Kd^{Eu2+}_{feldspar/monazite}$ is >>1. We propose that changes in $Eu/Eu^*_{monazite}$ could also be the result of changes in Eu^{2+}/Eu^{3+}, because of the difference in size and charge between Eu^{2+} and Eu^{3+} (Shannon, 1976). The experiments of Burnham et al. (2015) demonstrated that constant Eu^{3+}/Eu^{total} in silicate melts has a temperature dependence parallel to the quartz–fayalite–magnetite (QFM) buffer. Although the exact value of Eu^{3+}/Eu^{total} depended on melt composition in their experiments,

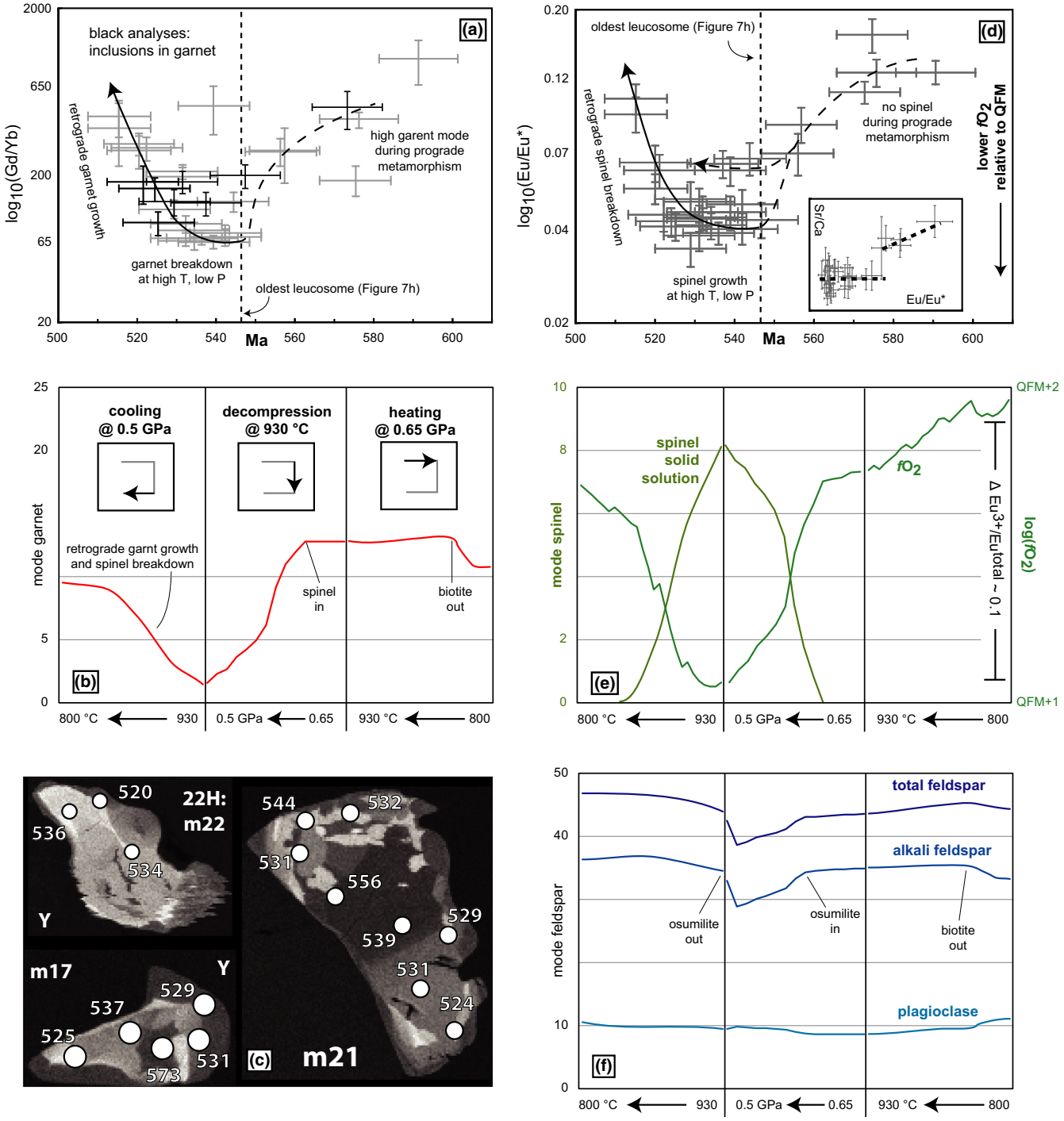

FIGURE 8 Monazite compositions reflect changes in the mode of garnet and bulk-rock fO_2 during metamorphism. Data are from sample 22H. (a) Gd/Yb in monazite record garnet breakdown during heating and garnet growth during cooling, consistent with petrographic observation in Figure 3 and garnet modes (b) calculated from a plausible clockwise *P–T* path extracted from pseudosections in Figure 5. (c) Y zoning in individual monazite grains shows low-Y cores, high-Y mantles and low-Y rims, consistent with Gd/Yb trends in *a*: high Gd/Yb corresponds to low Y. (d) Eu/Eu* decreases prior to 550 Ma, then increases, but is not correlated with Sr/Ca as expected for partitioning if bulk-rock Eu^{2+}/Eu^{3+} was constant. (e) fO_2 decreases, then increases along the *P–T* path proposed in Figure 7a due to changes in mode and composition of spinel. Changes in fO_2 relative to QFM result in corresponding changes in $Eu^{3+}/Eu^{total}_{rock}$ (Burnham et al., 2015) and might explain the observed trends in $Eu/Eu^*_{monazite}$, but lack of a correlation between Eu/Eu* and Sr/Ca. See text for more details. (f) Total feldspar decreases towards higher temperatures and lower pressures as a result of partial melting. It has been hypothesized that feldspar breakdown during partial melting should be recorded as an increase in monazite Eu/Eu* (e.g. Rubatto et al., 2006); the opposite is observed for the gneisses of south Madagascar, further supporting the novel hypothesis that monazite Eu/Eu* can reflect changes in fO_2

the results suggest that relative changes in Eu^{3+}/Eu^{total} can be inferred from changes in fO_2 relative to QFM (for convenience, all mentions of fO_2 in the following paragraphs are relative to QFM).

Whether changes in bulk-rock fO_2 are recorded by monazite Eu/Eu* can be tested by comparing monazite Eu/Eu* with Sr or Sr/Ca (normalizing to Ca removes the effect of the brabantite substitution—[Ca,Sr]Th↔2REE—on monazite Sr concentration). If Eu^{3+}/Eu^{total} remained constant during metamorphism (fO_2 remained constant), changes in $Eu/Eu^*_{monazite}$ should be positively correlated with changes in $Sr/Ca_{monazite}$ because Sr^{2+} and Eu^{2+} have nearly identical ionic radii (Shannon, 1976) and will therefore be equally compatible in each phase. If $Eu/Eu^*_{monazite}$ and $Sr/Ca_{monazite}$ are not correlated, the data may indicate changes in fO_2 and Eu^{3+}/Eu^{total} during metamorphism.

In sample 22H, $Sr/Ca_{monazite}$ is positively correlated with $Eu/Eu^*_{monazite}$ at $Eu/Eu^*_{monazite} > 0.1$, but shows no correlation at $Eu/Eu^*_{monazite} < 0.1$. The positive correlation at $Eu/Eu^*_{monazite} > 0.1$ is not robust, being strongly influenced by a single outlier datum (Figure 8d). The lack of robust correlation between $Sr/Ca_{monazite}$ and $Eu/Eu^*_{monazite}$ is compatible with changes in $Eu/Eu^*_{monazite}$ having been influenced by changes in fO_2.

Changes in fO_2 can result from fluid–rock interaction (open system) or from changes in mineral assemblage in unbuffered rocks (closed system). The magnitude of open-system modification of fO_2 in the osumilite gneisses cannot be constrained. To test how much bulk-rock fO_2 and monazite Eu/Eu* might have changed from closed-system metamorphism (from changes in pressure and temperature only), the pseudosection of sample 22H was contoured for μO_2, an intensive variable defined by the compositions and proportions of the Fe^{2+}–Fe^{3+}-bearing solid solutions (garnet, biotite, ilmenite and spinel in our pseudosection). The fO_2 was calculated from μO_2 along the proposed *P–T* path using the relationship $fO_{2(T,P)} = \exp([\mu O_{2(T,P)} - \mu O_{2(T,1bar,\ pure\ O_2)}]/RT)$; Figure 8e). Along this path, fO_2 decreased during heating and decompression and increased during cooling; the total magnitude of the change is ~1 $\log_{10}$ unit. The largest change in fO_2 is correlated with the growth and breakdown of spinel (Figure 8e). The exact relationship between fO_2, *T* and Eu^{3+}/Eu^{total} is not known for this type of rock; however, the experiments of Burnham et al. (2015) on silicate melts suggest that one $\log_{10}$ unit change in fO_2 is sufficient to change Eu^{3+}/Eu^{total} by 0.05–0.15 (higher fO_2 = higher Eu^{3+}/Eu^{total}); this is similar to the total variation in monazite Eu/Eu* observed in sample 22H (0.12).

In summary, $Eu/Eu^*_{monazite}$ has been interpreted as a record of feldspar growth and breakdown, but fO_2 likely plays a role too in some systems. $Eu/Eu^*_{monazite}$ from sample 22H does not correlate with $Sr_{monazite}$ (or Sr/Ca) as expected for partitioning in a system with constant Eu^{3+}/Eu^{total}. Modelled changes in fO_2 along the proposed *P–T* path may correspond to sufficient changes in $Eu^{3+}/Eu^{total}_{rock}$ to explain the observed variation in $Eu/Eu^*_{monazite}$. The modelled changes in fO_2 were a function of pressure, temperature and mineral assemblage only; the largest changes in fO_2 corresponded to the growth and breakdown of spinel. Open-system fluid–rock interaction might also influence bulk-rock fO_2 and therefore Eu/Eu*, but changes in fO_2 as a result of fluid–rock interaction are likely to be small in most metamorphic environments due to the large buffering capacity of rocks (Dyar, Lowe, Guidotti, & Delaney, 2002; Rumble, 1978).

5.2 | U–Pb LASS zircon

Zircon grains in the majority of samples are <30 μm across and only a few grains were found in most samples. One exception to this is osumilite gneiss 23A, in which several 100 μm zircon grains occur in association with a retrograde biotite corona around magnetite and ilmenite (Figure 9). The grains contain oscillatory zoned cores, CL-dark mantles and CL-bright rims. U–Pb analyses from grain cores define a discordia between 1,900–1,800 and 600–500 Ma. Concordant mantle and rim analyses are 580–520 Ma, similar to monazite dates (above), but the ubiquity of an inherited component, and the lack of any trends in zircon composition make the *P–T* significance of the dates unclear. The Ti-in zircon temperatures (Ferry & Watson, 2007) have a weighted average of 790 ± 8°C and there is no correlation between Ti concentrations and U–Pb dates. Either the zircon grains were not in equilibrium with the other phases in the rock (possibly due to their position in the now-former osumilite) or they did not grow/recrystallize at UHT. A similar lack of compositional equilibrium during resetting of zircon U–Pb dates has been documented in the granulites of Blanský Les in the Bohemian Massif (Štípská, Powell, Hacker, Holder, & Kylander-Clark, 2016). All monazite from this sample is isotopically homogeneous: 561 ± 6 Ma (Figure 7h).

6 | DISCUSSION

6.1 | Duration of heating and cooling

We infer prograde metamorphism in the Anosyen Domain of southern Madagascar to have lasted <29 ± 8 Ma based on the differences between the oldest monazite dates from all samples (579 ± 5 Ma) and the oldest monazite interpreted to have formed from melt crystallization (550 ± 6 Ma; Figure 10; see Section 5.1.1 for discussion and evaluation of the data). The difference in melt crystallization age and the age of monazite inclusions in osumilite

at the same outcrop (sample 23A) constrains the residence time of the rocks near the peak metamorphic temperature (~930°C) to have been <11 ± 8 Ma.

The U/Th–He monazite dates (530–510 Ma) from the gigantic monazite at Manangotry Pass indicate that the rocks took *c.* 30 Ma to cool to 400°C (Montel et al., 2018): an average cooling rate of 17 ± 7°C/Ma. The Sm–Nd garnet–zircon–monazite–whole-rock isochron date of 588 ± 13 Ma, reported by Paquette et al. (1994) from an Al-spinel–quartz gneiss, corresponds with the time of prograde metamorphism inferred in this study and the emplacement of the early plutons of the Anosyen Batholith (Figure 10), which also preserve Sm–Nd isochron dates consistent with prograde to peak metamorphism (*c.* 570–560 Ma). Smit, Scherer, and Mezger (2013) have suggested that preservation of Sm–Nd dates through a UHT event requires short residence time at UHT and cooling rates of 20 to >100°C/Ma through the granulite facies, an interpretation that is consistent with the short duration of peak metamorphism estimated in this study and the cooling rates constrained by the monazite U/Th–He dates described above.

The short duration of prograde metamorphism, short residence time at peak temperature and potentially rapid cooling rates all suggest that advection of heat may have been important for the formation of the osumilite gneisses. However, the interpretation that metamorphism was the result of continental collision and the overall long duration of the metamorphic event—recorded by monazite and zircon within the gneisses—is compatible with radiogenic heating within a long-lived thick crust. Below, we discuss the relative importance of advected and radiogenic heat.

6.2 | Can metamorphism be explained by high radiogenic heat production within thickened crust and no advection?

Horton et al. (2016) and Clark et al. (2015) proposed that UHTM in southern Madagascar and southern India might have been caused by the accumulation of radiogenic heat in the middle to lower crust if a 60–70 km thick crust was maintained for *c.* 60 Ma and if the crust contained an anomalously high concentration of the heat-producing elements U, Th and K. Measured high heat-production rates from gneisses in these terranes and long durations of metamorphism were cited as support for this hypothesis. The models of Horton et al. (2016) were particularly thorough, demonstrating the sensitivity of crustal temperatures to the distribution of heat-producing elements, thermal conductivity, mantle heat flow and erosion rates.

The means and 95% confidence intervals of heat-production rates from regional whole-rock data (taken from GAF-BGR 2008 and U, Th and K concentrations corrected to 600 Ma) for all the tectonometamorphic domains of southern Madagascar are plotted against the ratio of peak metamorphic temperature at peak metamorphic pressure (Figure 11). For terranes in which isothermal decompression has been inferred, the *P–T* conditions prior to decompression were used. Uncertainties in temperature and pressure were taken to be 50°C and 0.1 GPa. The highest average heat-production rate, ~3.5 μW/m³, is associated with the highest *T/P* metamorphic rocks (Anosyen and Antananarivo domains). The *T/P* of metamorphism is correlated with heat-production rates at the terrane scale. To test the magnitude of heating that might have resulted from radioactive decay within a thickened crust, one-dimensional lithospheric heat flow models were constructed, which are described briefly below and more thoroughly in Appendix S1.

We calculated relaxation of the thermal gradient of the crust following thickening from 30 to 60 km using one-dimensional finite-difference heat flow models for three high heat-production profiles: a homogeneous crust with a heat-production rate of 2 μW/m³, a homogeneous crust with a heat-production rate of 3 μW/m³, and the heat-production profile used by Horton et al. (2016) for the southern Anosyen domain. General details of the modelling approach were described by Peacock (1989). Specific model parameters are outlined in Appendix S1; heat-production profiles for each model are shown in Table S7.

Figure 12a shows the crustal thermal gradient 40 Ma after thickening (the maximum duration of prograde metamorphism from this study: <29 ± 8 Ma) for each model—using a "typical" mantle lithosphere thickness of 140 km—compared to the peak *P–T* estimates and *P–T* paths from this study, Jöns and Schenk (2011), and Boger et al. (2012). Only the models with average crustal heat-production ≥3 μW/m³ reached the peak *P–T* conditions proposed by these studies.

Figure 12b shows the time required to heat the crust to 930°C at a depth of 25 km (~0.65 GPa; corresponding to the pressure estimates of this study and Boger et al.) as a function of mantle lithosphere thickness (proximity of the lower crust to the convecting mantle) for each of the models. Temperatures of 930°C at 25 km depth are only reached in the models if heat-production rates are >3 μW/m³ and the mantle lithosphere is <80 km thick. Such a thin mantle lithosphere may not be unreasonable for a collisional orogen. UHT lower crustal xenoliths have been documented in Qiangtang, Tibet (Hacker et al., 2000), directly overlying mantle with anomalously slow seismic wave speeds (e.g. Liang et al., 2012; McNamara, Walter, Owens, & Ammon, 1997). The low wave speeds have been interpreted to reflect a thin lithospheric mantle (40–80 km thick; e.g. Jiménez-Munt, Fernàndez, Vergés, & Platt, 2008; Tunini et al., 2016) and possibly asthenospheric upwelling following lithospheric foundering

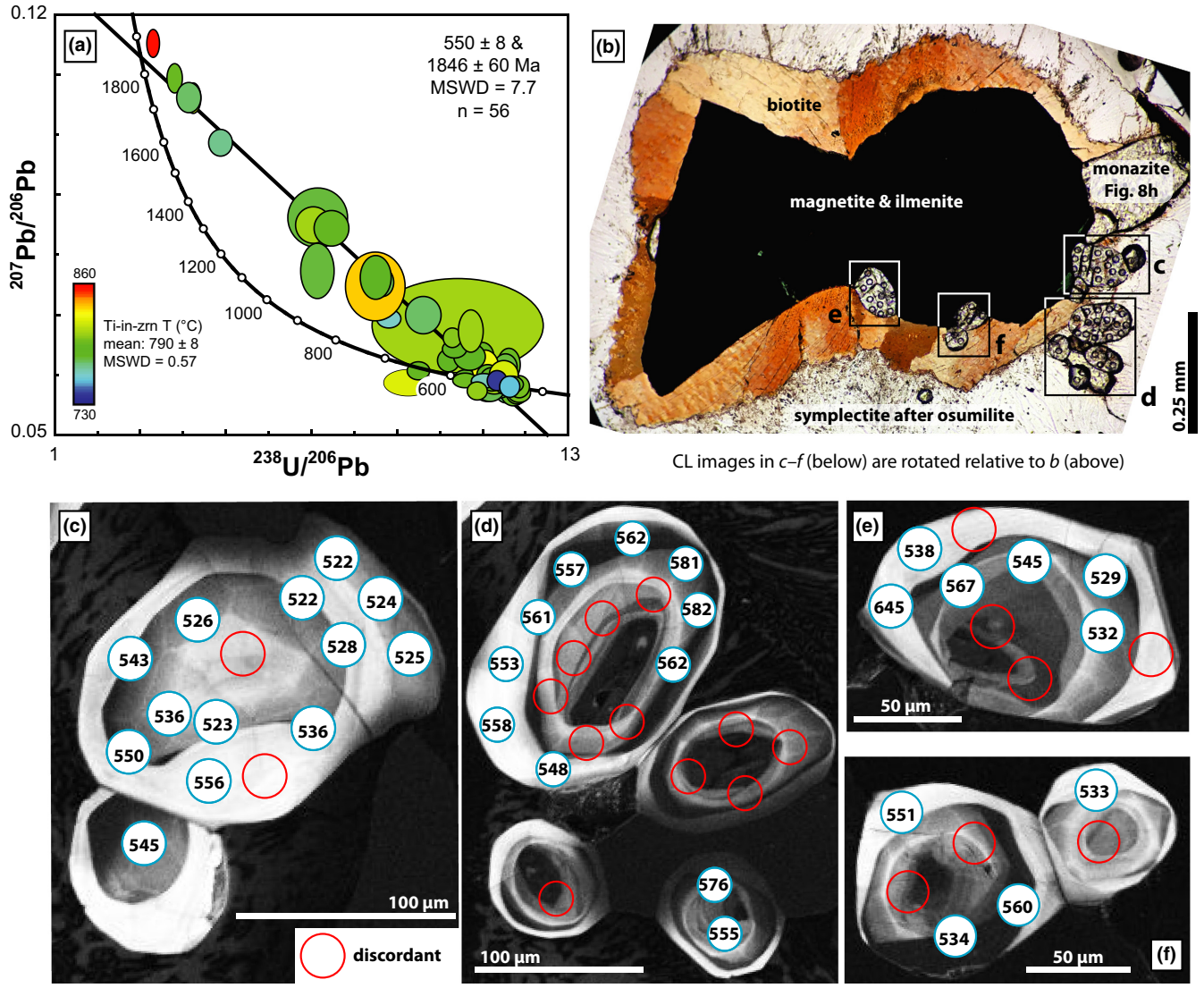

FIGURE 9 (a) U–Pb zircon dates in osumilite gneiss 23A define a discordia between 1,850 and 550 Ma. Ti-in-zircon temperatures have an average value of 790°C and are not correlated with date (see online version for analyses coloured by Ti concentration). (b) Optical photomicrograph showing association of zircon with retrograde biotite corona on magnetite and ilmenite. Monazite grains from the sample are isotopically homogeneous: 561 ± 6 Ma (Figure 8h). (c–f) CL images of zircon in *b* with LA-ICP-MS spot locations and ^{238}U–^{206}Pb dates (CL images have been rotated relative to *b* to better fit on page). Dates from zircon cores are discordant. CL-dark mantles and CL-bright rims are 590–520 Ma

(e.g. Jiménez-Munt & Platt, 2006; Liang et al., 2012; Molnar, England, & Martinod, 1993).

6.3 | How important were advective heat sources?

The short time-scales of heating (<29 ± 8 Ma), preservation of Sm–Nd dates from prograde to peak metamorphism, the location of osumilite gneisses around the Anosyen Batholith (Figure 1), emplacement dates for many of the high-*T* plutons within the Anosyen Batholith during prograde to peak metamorphism (Figure 10; Section 2.2), the low pressure of regional metamorphism (~0.6 GPa: Boger et al., 2012; this study) and the extreme heat-production rates required throughout the crust to reproduce metamorphic *P-T* estimates in models (Figure 12a,b and Section 6.2)—all suggest that advective heat sources might have been important in the thermal evolution of the southeastern Anosyen domain.

6.3.1 | High-*T* melt transfer within the crust

The Anosyen Batholith consists of >80% anhydrous granitoids and is the largest pre- to syn-tectonic body of the Ambalavao suite (GAF-BGR, 2008). In this section, we more generally refer to all of the plutons in southeast Madagascar as the Anosyen Batholith. The majority of dates from the Batholith are 570–560 Ma with a lesser number at *c.* 530 Ma (Section 2.2 and Figure 10); the

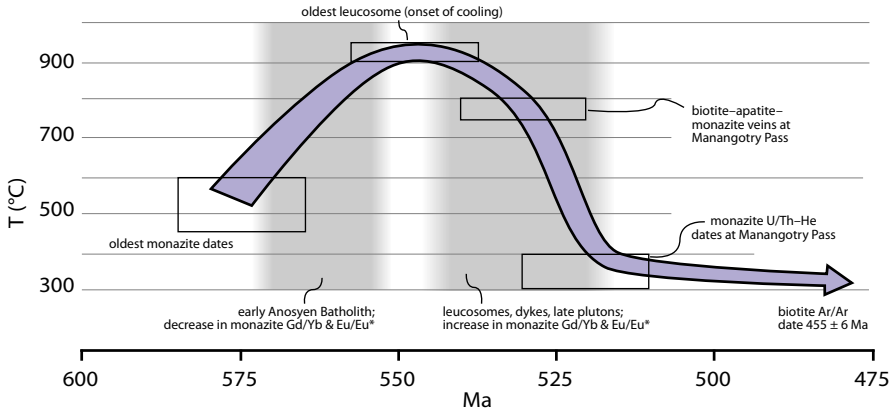

FIGURE 10 Temperature-time path of the Anosyen domain near Tranomaro and Tôlanaro from U/Th–Pb monazite dates of osumilite gneisses (this study), U/Th–Pb and U/Th–He monazite dates from Manangotry Pass (Montel et al., 2018), magmatic dates (see text for references), and Ar/Ar biotite dates from Manangotry Pass (Montel et al., 2018); the average cooling rate is 17 ± 7°C/Ma for 550–520 Ma

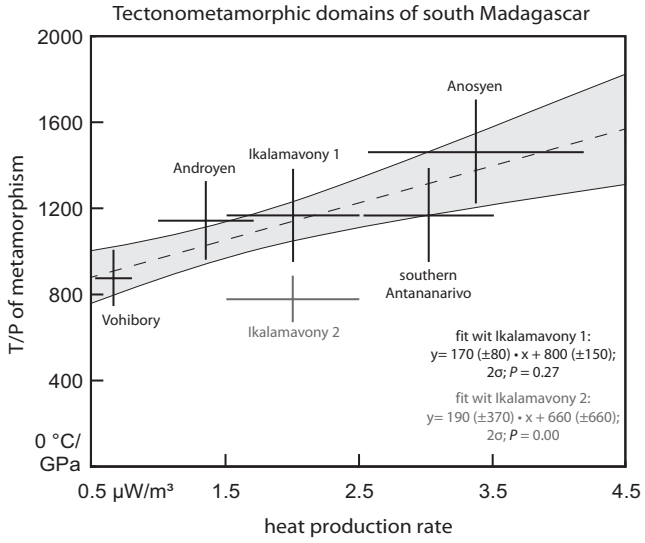

FIGURE 11 Average heat-production rate of southern Malagasy terranes correlates with the apparent thermal gradient of metamorphism (metamorphic temperature divided by metamorphic pressure). Decay of U, Th and K was an important heat source for high-grade metamorphism at the terrane scale (*P–T* data from GAF-BGR 2008; Grégoire et al. 2009; Jöns & Schenk 2008; Martelat et al. 1997; and this study)

mode of dates from the Batholith correlates with the timing of prograde to peak metamorphism. Isotopic data on the Batholith are limited to three whole-rock Nd isotope measurements of granites compatible with formation from crustal melting (Paquette et al., 1994); however, gabbro and quartz monzonite with trace-element composition distinct from the granites (no isotopic data is available) suggest some of the magmas had a different source (GAF-BGR, 2008), possibly the mantle. Hercynitic spinel in some of the granitoids indicates emplacement temperatures in the granulite facies. Orthopyroxene granitoids ("charnockites") were likely emplaced at temperatures of 950–1,050°C (Frost & Frost, 2008; Kilpatrick & Ellis, 2011); this generalization is corroborated by modelling the crystallization of these orthopyroxene granitoids in rhyoliteMELTS (Appendix S2), which suggests magmatic temperatures of 1,000–1,100°C. The high magmatic temperatures estimated for the plutons, and large extent of the Batholith (Figure 2), suggest that magmatic advection may have been an important heat source for metamorphism in the surrounding gneisses.

To investigate the potential magnitude of heating caused by the Anosyen Batholith, we calculated the minimum volume of magma required to heat a metamorphic terrane to 930°C using the following energy balance:

$$(930 - T_c)C_{pc}V_c\rho_c = V_m\rho_m((T_m - 930)C_{pm} + L)$$

T_c is the temperature of the crust into which the magma is emplaced, C_{pc} the heat capacity of the crust, ρ_c the density of the crust, V_c the volume of crust into which the magma is emplaced, V_m the volume of the magma, ρ_m the magma density, T_m is the emplacement temperature of the magma, C_{pm} the heat capacity of the magma and L the latent heat of crystallization of the magma. For simplicity, the density of the magma and the crust were assumed to be the same; C_{pc} = 1.25 J/gK; C_{pm} = 1.5 J/gK; and L = 300 J/g.

The volume of magma calculated this way is a minimum, because (1) if the magma is emplaced over a period of time rather than instantaneously, conduction causes cooling; (2) the latent heat of crystallization for the crustal rocks is neglected, because the fertility of the rocks at the time of magma emplacement is unknown; and (3) not all of the batholith was emplaced during prograde metamorphism (Figure 10; Section 2.2). Emplacement of magma over a millions of years, rather than instantaneously, results in smaller magnitude, but longer lived heating (Chapman & Furlong, 1992).

The results of these calculations are shown in Figure 12c. The peak temperatures for the Anosyen domain >100 km away from the Batholith (800–850°C: Boger et al., 2012; Raith et al., 2008) were used as the possible temperature of the crust into which the magmas intruded. We used half the area proportion of the Batholith currently exposed as the volume proportion of intruded magma; only half the aerial

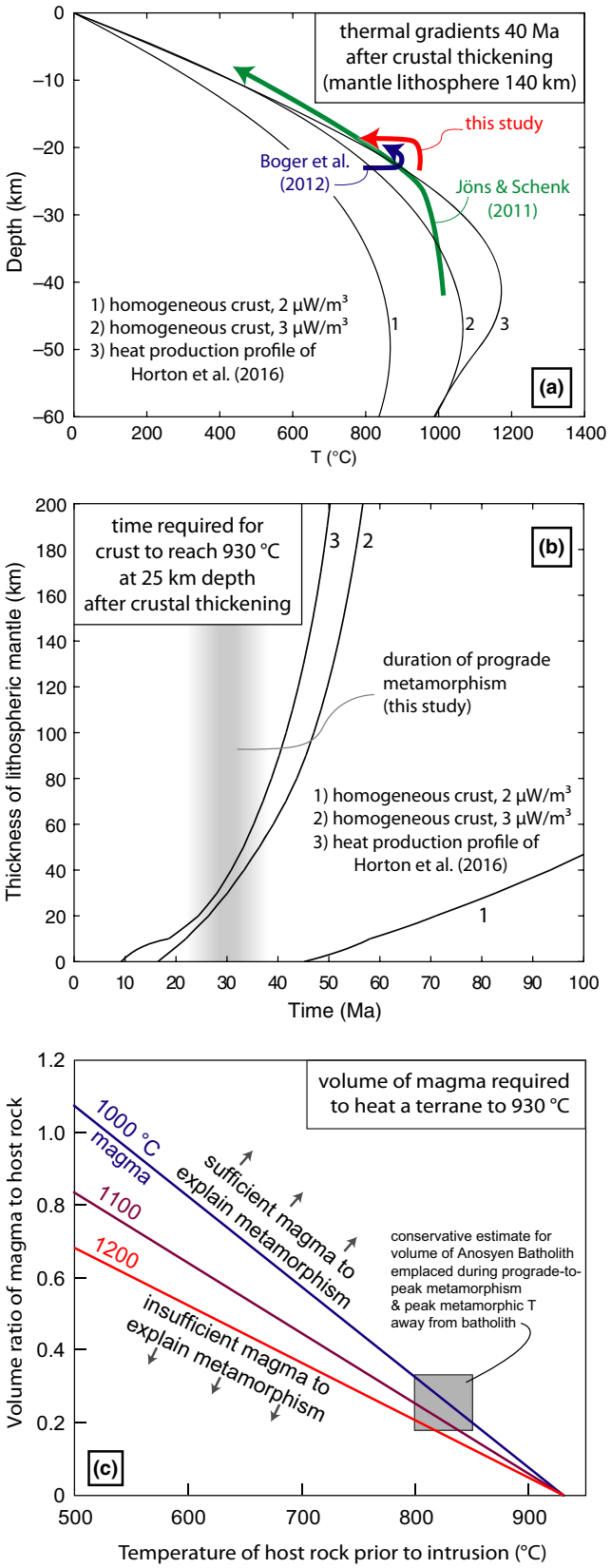

FIGURE 12 Models of plausible heat sources for UHTM in the Anosyen domain. (a) Model thermal gradients for crust with high radiogenic heat-production rates—and no advective heat transfer—40 Ma after crustal thickening from 30 to 60 km (duration of heating constrained by monazite dates; this study). Average crustal heat-production rates ≥3 μW/m³ are necessary for models to reproduce the *P–T–t* estimates of this study, Boger et al. (2012), and Jöns and Schenk (2011; see Section 6.1 and Appendix S1 for model details). (b) Same models as A, showing the influence of mantle lithosphere thickness on the temperature-time evolution of the crust at 25 km depth. The short duration of prograde metamorphism estimated in this study is best fit with a mantle lithosphere thickness less than 80 km and a highly radiogenic crust. Similarly, thin mantle lithosphere is inferred beneath modern central Tibet (e.g. Jiménez-Munt et al., 2008; Tunini et al., 2016). (c) Energy balance calculations showing the volume of magma required to heat a terrane to 930°C as a function of magma temperature and host-rock temperature prior to intrusion. The volume of the Anosyen Batholith may have been sufficient to explain the difference in peak metamorphic temperature between gneiss with osumilite near the batholith (~930°C) and gneisses without osumilite far away from the batholith (800–850°C). While advection of heat by magmatism is unlikely to have been the dominant source of heat for regional metamorphism, it may have been a locally important addition to the high rates of radiogenic heat production. See text Section 6.3.1 for further information

extent of the Batholith was used in the calculations to provide a conservative estimate for the magnitude of heating, in recognition of younger dates reported for some of the plutons (Section 2.2). If the calculated emplacement temperatures of the orthopyroxene granites are representative of the batholith, the Anosyen Batholith is large enough to explain the differences in peak metamorphic temperature across the domain —930°C near the batholith (this study) and 800–850°C near Ihosy (Boger et al., 2012; Raith et al., 2008)—but the Batholith is not large or extensive enough to have been the only heat source for metamorphism. This is supported by recognition of very high temperatures (~900°C) recorded by Zr-in-rutile (Horton et al., 2016) and Fe^{3+}-rich sapphirine-bearing rocks (Jöns & Schenk, 2011; Wheller et al., 2015) near the western margin of the domain, ~60 km from the batholith. Additional, mantle-derived heat sources that may have contributed to crustal melting and metamorphism are discussed below.

6.3.2 | Mantle-derived heat sources: Mafic magmatism and asthenospheric upwelling

Although minor, gabbro within the Anosyen Batholith suggests that mafic magmatism (and associated asthenospheric upwelling) may have contributed to heating the Anosyen domain. The similarities in major- and trace-element ratios in the gabbro and the much more abundant quartz monzonites of the Batholith (GAF-BGR, 2008) and the low densities of the exposed gneisses (2.7–2.8 g/cm³ calculated from the pseudosections of this study) suggest that mafic (denser) plutons may be more abundant at depth (Glazner,

1994). The thermal significance of mafic magmatism may be underestimated by the current exposure. Mantle-sourced heating is also suggested by oxygen and carbon isotopes of marbles, calcsilicates and metamafic rocks from the largest regional shear zones (such as the Beraketa shear zone that separates the Anosyen and Androyen domains, Figure 1; Pili, Sheppard, Lardeaux, Martelat, & Nicollet, 1997) which suggest mantle-derived fluids entered the crust during orogenesis, possibly associated with mafic magmatism or lithospheric thinning (Pili, Ricard, Lardeaux, & Sheppard, 1997). Despite the scarcity of exposed mafic plutons, it cannot be ruled out that mafic magmatism and/or asthenospheric upwelling contributed significant heat to the terrane.

7 | CONCLUSIONS

The Anosyen domain of southeast Madagascar was metamorphosed at ~930°C/0.6 GPa along a clockwise *P–T* path. At the 100s-of-km scale, metamorphic grade correlates with average heat-production rate, indicating that radioactive decay of U, Th and K was the main heat source for high-grade metamorphism. Models of heat flow and radiogenic heat production within thickened crust (without advection) require an average crustal heat-production rate of >3 μW/m³ and a mantle lithosphere thickness of <80 km to reproduce the *P–T* conditions experienced by the gneisses within the time permitted by monazite petrochronology (<29 ± 8 Ma).

Advective heating may also have been important. The volume and distribution of high-*T* plutons of the Anosyen Batholith are sufficient to explain differences in peak temperature across the domain (~930°C near the Anosyen Batholith and 800–850°C near Ihosy), but the processes that led to the generation of the plutons in the Batholith remain unclear. Isotopic data on the Batholith are limited to three whole-rock Nd isotope measurements compatible with formation from crustal melting (Paquette et al., 1994), highlighting the potential importance of intracrustal mass and heat transfer in the formation of low-*P* granulite UHT terranes. Minor mafic plutons and geochemically associated quartz monzonite (GAF-BGR, 2008), along with mantle-sourced carbon and oxygen isotopes from rocks within major shear zones (Pili, Ricard, et al., 1997; Pili, Sheppard, et al., 1997), suggest that mantle-sourced heat (mafic magmatism or asthenospheric upwelling) may have also been important despite the scarcity of mafic plutons exposed.

ACKNOWLEDGEMENTS

N. Jöns generously let us use his samples at the beginning of this study—including sample MD69 from this paper—which helped guide the initial stages of our work. Reviewers N. Jöns and S. Boger provided helpful comments and suggestions on the manuscript. J. Cottle, F. Spera, and R. Rudnick provided comments and suggestions on early drafts of the manuscript. A. Benisek gave advice concerning feldspar thermometry. Funded by the University of California, Santa Barbara and NSF-EAR-1348003.

ORCID


Robert M. Holder http://orcid.org/0000-0002-1119-6905

REFERENCES

Ackermand, D. (1991). Kornerupine breakdown reactions in paragneisses from Southern Madagascar. *Mineralogical Magazine*, *55* (378), 71–80. https://doi.org/10.1180/minmag.1991.055.378.06

Ackermand, D., Windley, B. F., & Razafiniparany, A. (1989). The Precambrian mobile belt of southern Madagascar. *Geological Society, London, Special Publications*, *43*(1), 293–296. https://doi.org/10.1144/GSL.SP.1989.043.01.20

Arima, M., & Gower, C. F. (1991). Osumilite-bearing granulites in the Eastern Grenville Province, eastern Labrador, Canada: Mineral parageneses and metamorphic conditions. *Journal of Petrology*, *32*(1), 29–61. https://doi.org/10.1093/petrology/32.1.29

Armbruster, T., & Oberhaesnsli, R. (1988). Crystal chemistry of double-ring silicates: Structural, chemical, and optical variation in osumilites. *American Mineralogist*, *73*(5–6), 585–594.

Baldwin, J. A., Powell, R., White, R. W., & Štípská, P. (2015). Using calculated chemical potential relationships to account for replacement of kyanite by symplectite in high pressure granulites. *Journal of Metamorphic Geology*, *33*, 311–330. https://doi.org/10.1111/jmg.12122

Bartoli, O. (2017). Phase equilibria modelling of residual migmatites and granulites: An evaluation of the melt-reintegration approach. *Journal of Metamorphic Geology*, *35*(8), 919–942. https://doi.org/10.1111/jmg.12261

Bea, F. (2012). The sources of energy for crustal melting and the geochemistry of heat-producing elements. *Lithos*, *153*(2012), 278–291. https://doi.org/10.1016/j.lithos.2012.01.017

Benisek, A., Dachs, E., & Kroll, H. (2010). A ternary feldspar-mixing model based on calorimetric data: Development and application. *Contributions to Mineralogy and Petrology*, *160*, 327–337. https://doi.org/10.1007/s00410-009-0480-8

Benisek, A., Kroll, H., & Cemič, L. (2004). New developments in two-feldspar thermometry. *American Mineralogist*, *89*(10), 1496–1504. https://doi.org/10.2138/am-2004-1018

Berg, J. H., & Wheeler, E. P. (1976). Osumilite of deep-seated origin in the contact aureole of the anorthositic Nain Complex, Labrador. *American Mineralogist*, *61*(1–2), 29–37.

Blereau, E., Clark, C., Taylor, R. J. M., Johnson, T. E., Fitzsimons, I. C. W., & Santosh, M. (2016). Constraints on the timing and conditions of high-grade metamorphism, charnockite formation, and fluid-rock interaction in the Trivandrum Block, southern India. *Journal of Metamorphic Geology*, *34*(6), 527–549. https://doi.org/10.1111/jmg.12192

Boger, S. D., Hirdes, W., Ferreira, C. A. M., Jenett, T., Dallwig, R., & Fanning, C. M. (2015). The 580–520 Ma Gondwana suture of Madagascar and its continuation into Antarctica and Africa. *Gondwana Research*, *28*(3), 1048–1060. https://doi.org/10.1016/j.gr.2014.08.017

Boger, S. D., Hirdes, W., Ferreira, C. A. M., Schulte, B., Jenett, T., & Fanning, C. M. (2014). From passive margin to volcano–sedimentary forearc: The Tonian to Cryogenian evolution of the Anosyen domain of southeastern Madagascar. *Precambrian Research*, *247*(2014), 159–186. https://doi.org/10.1016/j.precamres.2014.04.004

Boger, S. D., White, R. W., & Schulte, B. (2012). The importance of iron speciation (Fe^{+2}/Fe^{+3}) in determining mineral assemblages: An example from the high-grade aluminous metapelites of southeastern Madagascar. *Journal of Metamorphic Geology*, *30*(9), 997–1018. https://doi.org/10.1111/jmg.12001

Bohlen, S. R. (1987). Pressure-temperature-time paths and a tectonic model for the evolution of granulites. *The Journal of Geology*, *95*(5), 617–632. https://doi.org/10.1086/629159

Brown, M. (2006). Duality of thermal regimes is the distinctive characteristic of plate tectonics since the Neoarchean. *Geology*, *34*(11), 961. https://doi.org/10.1130/G22853A.1

Bunch, T. E., & Fuchs, L. H. (1969). Yagiite, a new sodium-magnesium analogue of osumilite. *American Mineralogist*, *54*, 14–18.

Burnham, A. D., Berry, A. J., Halse, H. R., Schofield, P. F., Cibin, G., & Mosselmans, J. F. W. (2015). The oxidation state of europium in silicate melts as a function of oxygen fugacity, composition and temperature. *Chemical Geology*, *411*, 248–259. https://doi.org/10.1016/j.chemgeo.2015.07.002

Carrington, D. P., & Harley, S. L. (1995). The stability of osumilite in metapelitic granulites. *Journal of Metamorphic Geology*, *13*, 613–625. https://doi.org/10.1111/j.1525-1314.1995.tb00246.x

Chapman, D. S., & Furlong, K. P. (1992). The thermal state of the continental lower crust. In Continental Lower Crust (Development in Geotectonics, vol. 23). Amsterdam; New York: Elsevier.

Chinner, G. A., & Dixon, P. D. (1973). Irish osumilite. *Mineralogical Magazine*, *39*(302), 189–192. https://doi.org/10.1180/minmag.1973.039.302.06

Clark, C., Fitzsimons, I. C. W., Healy, D., & Harley, S. L. (2011). How does the continental crust get really hot? *Elements*, *7*(4), 235–240. https://doi.org/10.2113/gselements.7.4.235

Clark, C., Healy, D., Johnson, T., Collins, A. S., Taylor, R. J., Santosh, M., & Timms, N. E. (2015). Hot orogens and supercontinent amalgamation: A Gondwanan example from southern India. *Gondwana Research*, *28*(4), 1310–1328. https://doi.org/10.1016/j.gr.2014.11.005

Collins, A. S., Kinny, P. D., & Razakamanana, T. (2012). Depositional age, provenance and metamorphic age of metasedimentary rocks from southern Madagascar. *Gondwana Research*, *21*(2–3), 353–361. https://doi.org/10.1016/j.gr.2010.12.006

Collins, A. S., & Windley, B. F. (2002). The tectonic evolution of Central and Northern Madagascar and its place in the final assembly of Gondwana. *The Journal of Geology*, *110*(3), 325–339. https://doi.org/10.1086/339535

Connolly, J. A. D. (2009). The geodynamic equation of state: What and how. *Geochemistry, Geophysics, Geosystems*, *10*(10), 1–19. https://doi.org/10.1029/2009GC002540

Das, K., Dasgupta, S., & Miura, H. (2001). Stability of osumilite coexisting with spinel solid solution in metapelitic granulites at high oxygen fugacity. *American Mineralogist*, *86*, 1423–1434. https://doi.org/10.2138/am-2001-11-1211

Dodd, R. T., Schmus, W. R. V., & Marvin, U. B. (1965). Merrihueite, a new alkali-ferromagnesian silicate from the Mezö-Madaras Chondrite. *American Journal of Science*, *149*(3687), 972–974.

Dooley, D. F., & Patiño Douce, A. E. (1996). Fluid-absent melting of F-rich phlogopite + rutile + quartz. *American Mineralogist*, *81*, 202–212. https://doi.org/10.2138/am-1996-1-225

Dyar, M. D., Lowe, E. W., Guidotti, C. V., & Delaney, J. S. (2002). Fe^{3+} and Fe^{2+} partitioning among silicates in metapelites: A synchrotron micro-XANES study. *American Mineralogist*, *87*, 514–522. https://doi.org/10.2138/am-2002-0414

Ferry, J. M., & Watson, E. B. (2007). New thermodynamic models and revised calibrations for the Ti-in-zircon and Zr-in-rutile thermometers. *Contributions to Mineralogy and Petrology*, *154*(4), 429–437. https://doi.org/10.1007/s00410-007-0201-0

Finch, E. G., & Tomkins, A. G. (2017). Fluorine and chlorine behaviour during progressive dehydration melting: Consequences for granite geochemistry and metallogeny. *Journal of Metamorphic Geology*, *35*, 739–757. https://doi.org/10.1111/jmg.12253

Frost, B. R., & Frost, C. D. (2008). On charnockites. *Gondwana Research*, *13*(1), 30–44. https://doi.org/10.1016/j.gr.2007.07.006

Fuchs, L. H., Frondel, C., & Klein, C. J. (1966). Roedderite, a new mineral from the Indarch meteorite. *American Mineralogist*, *51*, 949–955.

Fuhrman, M. L., & Lindsley, D. H. (1988). Ternary-feldspar modeling and thermometry. *American Mineralogist*, *73*, 201–215.

GAF-BGR. (2008). Explanatory notes for the Anosyen Domain, southeast Madagascar. Antananarivo:Republique de Madagascar, Ministère de L'energie et des Mines (MEM/SG/DG/UCP/PGRM).

Giese, J., Berger, A., Schreurs, G., & Gnos, E. (2011). The timing of the tectono-metamorphic evolution at the Neoproterozoic-Phanerozoic boundary in central southern Madagascar. *Precambrian Research*, *185*, 131–148. https://doi.org/10.1016/j.precamres.2011.01.002

Glazner, A. F. (1994). Foundering of mafic plutons and density stratification of continental crust. *Geology*, *22*(5), 435–438. https://doi.org/10.1130/0091-7613(1994) 022<0435:FOMPAD>2.3.CO;2

Grégoire, V., Nédélec, A., Monié, P., Montel, J.-M., Ganne, J., & Ralison, B. (2009). Structural reworking and heat transfer related to the late-Panafrican Angavo shear zone of Madagascar. *Tectonophysics*, *477*(3–4), 197–216. https://doi.org/10.1016/j.tecto.2009.03.009

Guevara, V. E., & Caddick, M. J. (2016). Shooting at a moving target: Phase equilibria modelling of high-temperature metamorphism. *Journal of Metamorphic Geology*, *34*(3), 209–235. https://doi.org/10.1111/jmg.12179

Hacker, B. R., Gnos, E., Ratschbacher, L., Webb, L., Grove, M., McWilliams, M., … Wu, Z. (2000). Hot and dry xenoliths from the lower crust of Tibet. *Science*, *287*, 2463–2466. https://doi.org/10.1126/science.287.5462.2463

Hacker, B. R., Ritzwoller, M. H., & Xie, J. (2014). Partially melted, mica-bearing crust in central Tibet. *Tectonics*, *33*(1), 1408–1424. https://doi.org/10.1002/2014TC003545

Harley, S. L. (2016). A matter of time: The importance of the duration of UHT metamorphism. *Journal of Mineralogical and Petrological Sciences*, *111*(2), 50–72. https://doi.org/10.2465/jmps.160128

Harlov, D. E., & Milke, R. (2002). Stability of corundum + quartz relative to kyanite and sillimanite at high temperature and pressure. *American Mineralogist*, *87*, 424–432. https://doi.org/10.2138/am-2002-0406

Holder, R. M., Hacker, B. R., Kylander-Clark, A. R. C., & Cottle, J. M. (2015). Monazite trace-element and isotopic signatures of (ultra)high-pressure metamorphism: Examples from the Western Gneiss Region, Norway. *Chemical Geology*, *409*, 99–111. https://doi.org/10.1016/j.chemgeo.2015.04.021

Holland, T. J. B., Babu, E. V. S. S. K., & Waters, D. J. (1996). Phase relations of osumilite and dehydration melting in pelitic rocks: A simple thermodynamic model for the KFMASH system. *Contributions to Mineralogy and Petrology*, *124*, 383–394. https://doi.org/10.1007/s004100050198

Holland, T. J. B., & Powell, R. (2011). An improved and extended internally consistent thermodynamic dataset for phases of petrological interest, involving a new equation of state for solids. *Journal of Metamorphic Geology*, *29*(3), 333–383. https://doi.org/10.1111/j.1525-1314.2010.00923.x

Horton, F., Hacker, B. R., Kylander-Clark, A. R. C., Holder, R. M., & Jöns, N. (2016). Focused radiogenic heating of middle crust caused ultrahigh temperatures in southern Madagascar. *Tectonics*, *35*, 293–314. https://doi.org/10.1002/2015TC004040

Hyndman, R. D., Currie, C. A., & Mazzotti, S. P. (2005). Subduction zone backarcs, mobile belts, and orogenic heat. *GSA Today*, *15*(2), 4–10. https://doi.org/10:1130/1052-5173(2005)015

Jaupart, C., Mareschal, J.-C., & Iarotsky, L. (2016). Radiogenic heat production in the continental crust. *Lithos*, *262*, 398–427. https://doi.org/10.1016/j.lithos.2016.07.017

Jiménez-Munt, I., Fernàndez, M., Vergés, J., & Platt, J. P. (2008). Lithosphere structure underneath the Tibetan Plateau inferred from elevation, gravity and geoid anomalies. *Earth and Planetary Science Letters*, *267*(1–2), 276–289. https://doi.org/10.1016/j.epsl.2007.11.045

Jiménez-Munt, I., & Platt, J. P. (2006). Influence of mantle dynamics on the topographic evolution of the Tibetan Plateau: Results from numerical modeling. *Tectonics*, *25*(6), 1–17. https://doi.org/10.1029/2006TC001963

Johnson, T. E., Clark, C., Taylor, R. J. M., Santosh, M., & Collins, A. S. (2015). Prograde and retrograde growth of monazite in migmatites: An example from the Nagercoil Block, southern India. *Geoscience Frontiers*, *6*(3), 373–387. https://doi.org/10.1016/j.gsf.2014.12.003

Jöns, N., & Schenk, V. (2011). The ultrahigh temperature granulites of southern Madagascar in a polymetamorphic context: Implications for the amalgamation of the Gondwana supercontinent. *European Journal of Mineralogy*, *23*(2), 127–156. https://doi.org/10.1127/0935-1221/2011/0023-2087

Jöns, N., & Schenk, V. (2008). Relics of the Mozambique Ocean in the central East African Orogen: Evidence from the Vohibory Block of southern Madagascar. *Journal of Metamorphic Geology*, *26*(1), 17–28. https://doi.org/10.1111/j.1525-1314.2007.00745.x

Kelsey, D. E. (2008). On ultrahigh-temperature crustal metamorphism. *Gondwana Research*, *13*(1), 1–29. https://doi.org/10.1016/j.gr.2007.06.001

Kelsey, D. E., & Hand, M. (2015). On ultrahigh temperature crustal metamorphism: Phase equilibria, trace element thermometry, bulk composition, heat sources, timescales and tectonic settings. *Geoscience Frontiers*, *6*(3), 311–356. https://doi.org/10.1016/j.gsf.2014.09.006

Kemp, A. I. S., Shimura, T., & Hawkesworth, C. J. (2007). Linking granulites, silicic magmatism, and crustal growth in arcs: Ion micropobe (zircon) U-Pb ages from the Hidaka metamorphic belt, Japan. *Geology*, *35*(9), 807–810. https://doi.org/10.1130/G23586A.1

Kilpatrick, J. A., & Ellis, D. J. (2011). C-type magmas: Igneous charnockites and their extrusive equivalents. *Transactions of the Royal Society of Edinburgh: Earth Sciences*, *83*(1–2), 155–164. https://doi.org/10.1017/S0263593300007847

Korhonen, F. J., Brown, M., Clark, C., & Bhattacharya, S. (2013). Osumilite-melt interactions in ultrahigh temperature granulites: Phase equilibria modelling and implications for the P-T-t evolution of the eastern ghats province, India. *Journal of Metamorphic Geology*, *31*(8), 881–907. https://doi.org/10.1111/jmg.12049

Kretz, R. (1983). Symbols for rock-forming minerals. *American Mineralogist*, *68*, 277–279.

Kroll, H., Evangelakakis, C., & Voll, G. (1993). Two-feldspar geothermometry: A review and revision for slowly cooled rocks. *Contributions to Mineralogy and Petrology*, *114*(4), 510–518. https://doi.org/10.1007/BF00321755

Kylander-Clark, A. R. C. (2017). Petrochronology by laser-ablation inductively coupled plasma mass spectrometry. *Reviews in Mineralogy and Geochemistry*, *83*, 183–196. https://doi.org/10.2138/rmg.2017.83.6

Kylander-Clark, A. R. C., Hacker, B. R., & Cottle, J. M. (2013). Laser-ablation split-stream ICP petrochronology. *Chemical Geology*, *345*, 99–112. https://doi.org/10.1016/j.chemgeo.2013.02.019

Liang, X., Sandvol, E., Chen, Y. J., Hearn, T., Ni, J., Klemperer, S., … Tilmann, F. (2012). A complex Tibetan upper mantle: A fragmented Indian slab and no south-verging subduction of Eurasian lithosphere. *Earth and Planetary Science Letters*, *333–334*, 101–111. https://doi.org/10.1016/j.epsl.2012.03.036

Martelat, J.-E., Lardeaux, J.-M., Nicollet, C., & Rakotondrazafy, R. (2000). Strain pattern and late Precambrian deformation history in southern Madagascar. *Precambrian Research*, *102*(1–2), 1–20. https://doi.org/10.1016/S0301-9268(99)00083-2

Martelat, J.-E., Malamoud, K., Cordier, P., Randrianasolo, B., Schulmann, K., & Lardeaux, J.-M. (2012). Garnet crystal plasticity in the continental crust, new example from south Madagascar. *Journal of Metamorphic Geology*, *30*, 435–452. https://doi.org/10.1111/j.1525-1314.2012.00974.x

Martelat, J.-E., Nicollet, C., Lardeaux, J. M., Vidal, G., & Rakotondrazafy, R. (1997). Lithospheric tectonic structures developed under high-grade metamorphism in the Southern part of Madagascar. *Geodinamica Acta*, *10*(3), 94–114.

Martelat, J.-E., Randrianasolo, B., Schulmann, K., Lardeaux, J.-M., & Devidal, J.-L. (2014). Airborne magnetic data compared to petrology of crustal scale shear zones from southern Madagascar: A tool for deciphering magma and fluid transfer in orogenic crust. *Journal of African Earth Sciences*, *94*, 74–85. https://doi.org/10.1016/j.jafrearsci.2013.07.003

Mattinson, J. M. (2005). Zircon U-Pb chemical abrasion ("CA-TIMS") method: Combined annealing and multi-step partial dissolution analysis for improved precision and accuracy of zircon ages. *Chemical Geology*, *220*, 47–66. https://doi.org/10.1016/j.chemgeo.2005.03.011

McDonough, W. F. & Sun, S.-S. (1995). The composition of the earth. *Chemical Geology*, *120*, 223–253. https://doi.org/10.1016/0009-2541(94)00140-4

McNamara, D. E., Walter, W. R., Owens, T. J., & Ammon, C. J. (1997). Upper mantle velocity structure beneath the Tibetan Plateau from Pn travel time tomography. *Journal of Geophysical Research*, *102*(B1), 493–505. https://doi.org/10.1029/96JB02112

Meert, J. G., & Lieberman, B. S. (2008). The Neoproterozoic assembly of Gondwana and its relationship to the Ediacaran-Cambrian radiation. *Gondwana Research*, *14*, 5–21. https://doi.org/10.1016/j.gr.2007.06.007

Molnar, P., England, P., & Martinod, J. (1993). Mantle dynamics, uplift of the Tibetan plateau, and the Indian monsoon. *Reviews of Geophysics*, *31*(4), 357–396. http://www.agu.org/pubs/crossref/1993/93RG02030.shtml https://doi.org/10.1029/93RG02030

Montel, J.-M., Razafimahatratra, D., de Parseval, P., Poitrasson, F., Moine, B., Seydoux-Guillaume, A.-M., … Gibert, F. (2018). The giant monazite crystals from Manangotry (Madagascar). *Chemical Geology*, *484*, 36–50. https://doi.org/10.1016/j.chemgeo.2017.10.034

Motoyoshi, Y., & Hensen, B. J. (2001). F-rich phlogopite stability in ultra-high-temperature metapelites from the Napier Complex, East Antarctica. *American Mineralogist*, *86*, 1404–1413. https://doi.org/10.2138/am-2001-11-1209

Mottram, C. M., Warren, C. J., Regis, D., Roberts, N. M. W., Harris, N. B. W., Argles, T. W., & Parrish, R. R. (2014). Developing an inverted barrovian sequence; insights from monazite petrochronology. *Earth and Planetary Science Letters*, *403*, 418–431. https://doi.org/10.1016/j.epsl.2014.07.006

Nabelek, P. I., Whittington, A. G., & Hofmeister, A. M. (2010). Strain heating as a mechanism for partial melting and ultrahigh temperature metamorphism in convergent orogens: Implications of temperature-dependent thermal diffusivity and rheology. *Journal of Geophysical Research: Solid Earth*, *115*(12), 1–17. https://doi.org/10.1029/2010JB007727

Nelson, K. D., Zhao, W., Brown, L. D., Kuo, J., Che, J., Liu, X., … Edwards, M. (1996). Partially molten middle crust beneath southern Tibet: Synthesis of project INDEPTH Results. *Science*, *274*, 1684–1688. https://doi.org/10.1126/science.274.5293.1684

Nichols, G. T., Berry, R. F., & Green, D. H. (1992). Internally consistent gahnitic spinel-cordierite-garnet equilibria in the FMASHZn system: Geothermobarometry and applications. *Contributions to Mineralogy and Petrology*, *111*(3), 362–377. https://doi.org/10.1007/BF00311197

Nicollet, C. (1985). Les gneiss rubanés à cordiérite et grenat d'ihosy: Un marqueur thermo-barométrique dans le sud de Madagascar. *Precambrian Research*, *28*(2), 175–185. https://doi.org/10.1016/0301-9268(85)90079-8

Olsen, E. (1967). A new occurence of roedderite and its bearing on osumilite-type minerals. *American Mineralogist*, *52*, 1519–1523.

Olsen, E., & Bunch, T. E. (1970). Compositions of natural osumilites. *American Mineralogist*, *55*, 875–879.

Paquette, J.-L., Nédélec, A., Moine, B., & Rakotondrazafy, A. F. M. (1994). U-Pb, single Zircon Pb-evaporation, and Sm-Nd isotopic study of a granulite domain in SE Madagascar. *The Journal of Geology*, *102*(5), 523–538. https://doi.org/10.1086/629696

Peacock, S. M. (1989). Thermal modeling of metamorphic pressure-temperature-time paths: A forward approach. In F. S. Spear & S. M. Peacock (Eds.), Metamorphic Pressure-Temperature-Time Paths. (pp. 57–102). Washington, D. C.: American Geophysical Union. https://doi.org/10.1029/SC007p0057

Pili, É., Ricard, Y., Lardeaux, J.-M., & Sheppard, S. M. F. (1997). Lithospheric shear zones and mantle-crust connections. *Tectonophysics*, *280*(1–2), 15–29. https://doi.org/10.1016/S0040-1951(97)00142-X

Pili, É., Sheppard, S. M. F., Lardeaux, J.-M., Martelat, J.-E., & Nicollet, C. (1997). Fluid flow vs. scale of shear zones in the lower continental crust and the granulite paradox. *Geology*, *25*(1), 15–18. https://doi.org/10.1130/0091-7613(1997) 025<0015:FFVSOS>2.3.CO;2

Pownall, J. M. (2014). Earth's youngest known ultrahigh-temperature granulites discovered on Seram, Eastern Indonesia. *Geology*, *42*(4), 279–282. https://doi.org/10.1130/G35230.1

Raith, M. M., Rakotondrazafy, R., & Sengupta, P. (2008). Petrology of corundum-spinel-sapphirine-anorthite rocks (sakenites) from the type locality in southern Madagascar. *Journal of Metamorphic Geology*, *26*(6), 647–667. https://doi.org/10.1111/j.1525-1314.2008.00779.x

Rakotonandrasana, N. O. T., Arima, M., Miyawaki, R., & Rambeloson, R. A. (2010). Widespread occurrences of hogbomite-2N2S in UHT metapelites from the Betroka Belt, Southern Madagascar: Implications on melt or fluid activity during regional metamorphism. *Journal of Petrology*, *51*(4), 869–895. https://doi.org/10.1093/petrology/egq004

Rakotondrazafy, A. F. M., Moine, B., & Cuney, M. (1996). Mode of formation of hibonite (CaAl12O19) within the U-Th skarns from the granulites of S-E Madagascar. *Contributions to Mineralogy and Petrology*, *123*(2), 190–201. https://doi.org/10.1007/s004100050150

Rubatto, D., Hermann, J., & Buick, I. S. (2006). Temperature and bulk composition control on the growth of monazite and zircon during low-pressure anatexis (Mount Stafford, Central Australia). *Journal of Petrology*, *47*(10), 1973–1996. https://doi.org/10.1093/petrology/egl033

Rumble, D. (1978). Mineralogy, petrology, and oxygen isotopic geochemistry of the Clough Formation, Mountain, W. New Hampshire, USA. *Journal of Petrology*, *19*, 317–340. https://doi.org/10.1093/petrology/19.2.317

Sandiford, M., & McLaren, S. (2002). Tectonic feedback and the ordering of heat producing elements within the continental lithosphere. *Earth and Planetary Science Letters*, *204*(1–2), 133–150. https://doi.org/10.1016/S0012-821X(02)00958-5

Sandiford, M., Mclaren, S., & Neumann, N. (2002). Long-term thermal consequences of the redistribution of heat-producing elements associated with large-scale granitic complexes. *Journal of Metamorphic Geology*, *20*(1), 87–98. https://doi.org/10.1046/j.0263-4929.2001.00359.x

Sandiford, M., & Powell, R. (1986). Deep crustal metamorphism during crustal extension: Modern and ancient examples. *Earth and Planetary Science Letters*, *79*, 151–158. https://doi.org/10.1016/0012-821X(86)90048-8

Sawyer, E. W., Cesare, B., & Brown, M. (2011). When the continental crust melts. *Elements*, *7*(4), 229–234. https://doi.org/10.2113/gselements.7.4.229

Schorn, S., & Diener, J. F. A. (2017). Details of the gabbro-to-eclogite transition determined from microtextures and calculated chemical potential relationships. *Journal of Metamorphic Geology*, *35*(1), 55–75. https://doi.org/10.1111/jmg.12220

Shannon, R. D. (1976). Revised effective ionic radii and systematic studies of interatomie distances in halides and chalcogenides. *Acta Crystallographica*, *A32*, 751–767.

Smit, M. A., Scherer, E. E., & Mezger, K. (2013). Lu-Hf and Sm-Nd garnet geochronology: Chronometric closure and implications for dating petrological processes. *Earth and Planetary Science Letters*, *381*, 222–233. https://doi.org/10.1016/j.epsl.2013.08.046

Spear, F. S. (2010). Monazite-allanite phase relations in metapelites. *Chemical Geology*, *279*(1–2), 55–62. https://doi.org/10.1016/j.chemgeo.2010.10.004

Stearns, M. A., Hacker, B. R., Ratschbacher, L., Lee, J., Cottle, J. M., & Kylander-Clark, A. R. C. (2013). Synchronous Oligocene-Miocene metamorphism of the Pamir and the north Himalaya driven by plate-scale dynamics. *Geology*, *41*(10), 1071–1074. https://doi.org/10.1130/G34451.1

Stepanov, A. S., Hermann, J., Rubatto, D., & Rapp, R. P. (2012). Experimental study of monazite/melt partitioning with implications for the REE, Th and U geochemistry of crustal rocks. *Chemical Geology*, *300–301*, 200–220. https://doi.org/10.1016/j.chemgeo.2012.01.007

Štípská, P., Powell, R., Hacker, B. R., Holder, R. M., & Kylander-Clark, A. R. C. (2016). Uncoupled U/Pb and REE response in zircon during the transformation of eclogite to mafic and intermediate granulite (Blanský les, Bohemian Massif). *Journal of Metamorphic Geology*, *34*(6), https://doi.org/10.1111/jmg.12193

Štípská, P., Powell, R., & Racek, M. (2014). Rare eclogite-mafic granulite in felsic granulite in Blanský les: Precursor of intermediate granulite in the Bohemian Massif? *Journal of Metamorphic Geology*, *32*(4), 325–345. https://doi.org/10.1111/jmg.12075

Štípská, P., Powell, R., Racek, M., & Lexa, O. (2014). Intermediate granulite produced by transformation of eclogite at a felsic granulite contact, in Blanský les, Bohemian Massif. *Journal of Metamorphic Geology*, *32*(4), 347–370. https://doi.org/10.1111/jmg.12079

Štípská, P., Powell, R., White, R. W., & Baldwin, J. A. (2010). Using calculated chemical potential relationships to account for coronas around kyanite: An example from the Bohemian Massif. *Journal of Metamorphic Geology*, *28*(1), 97–116. https://doi.org/10.1111/j.1525-1314.2009.00857.x

Taylor, R. J. M., Clark, C., Fitzsimons, I. C. W., Santosh, M., Hand, M., Evans, N., & McDonald, B. (2014). Post-peak, fluid-mediated modification of granulite facies zircon and monazite in the Trivandrum Block, southern India. *Contributions to Mineralogy and Petrology*, *168*(2), 1–17. https://doi.org/10.1007/s00410-014-1044-0

Tucker, R. D., Roig, J.-Y., Delor, C., Amelin, Y., Goncalves, P., Rabarimanana, M. H., … Belcher, R. W. (2011). Neoproterozoic extension in the Greater Dharwar Craton: A reevaluation of the "Betsimisaraka suture" in Madagascar. *Canadian Journal of Earth Sciences*, *48*(2), 389–417. https://doi.org/10.1139/E10-034

Tucker, R. D., Roig, J. Y., Macey, P. H., Delor, C., Amelin, Y., Armstrong, R. A., … Ralison, A. V. (2011). A new geological framework for south-central Madagascar, and its relevance to the "out-of-Africa" hypothesis. *Precambrian Research*, *185*(3–4), 109–130. https://doi.org/10.1016/j.precamres.2010.12.008

Tucker, R. D., Roig, J. Y., Moine, B., Delor, C., & Peters, S. G. (2014). A geological synthesis of the Precambrian shield in Madagascar. *Journal of African Earth Sciences*, *94*, 9–30. https://doi.org/10.1016/j.jafrearsci.2014.02.001

Tunini, L., Jiménez-Munt, I., Fernandez, M., Vergés, J., Villaseñor, A., Melchiorre, M., & Afonso, J. C. (2016). Geophysical-petrological model of the crust and upper mantle in the India-Eurasia collision zone. *Tectonics*, *35*(7), 1642–1669. https://doi.org/10.1002/2016TC004161

Wendt, I., & Carl, C. (1991). The statistical distribution of the mean squared weighted deviation. *Chemical Geology: Isotope Geoscience Section*, *86*(4), 275–285. https://doi.org/10.1016/0168-9622(91)90010-T

Wheller, C. J., Powell, R., White, R. W., & Boger, S. D.(2015). Conditions of formation for an oxidised sapphirine-bearing mineral assemblage from southern Madagascar. In Granulites & Granulites Conference.

White, R. W., Powell, R., & Baldwin, J. A. (2008). Calculated phase equilibria involving chemical potentials to investigate the textural evolution of metamorphic rocks. *Journal of Metamorphic Geology*, *26*(2), 181–198. https://doi.org/10.1111/j.1525-1314.2008.00764.x

White, R. W., Powell, R., & Clarke, G. L. (2002). The interpretation of reaction textures in Fe-rich metapelitic granulites of the Musgrave Block, Central Australia: Constraints from mineral equilibria calculations in the system. *Journal of Metamorphic Geology*, *20*(1), 41–55. https://doi.org/10.1046/j.0263-4929.2001.00349.x

White, R. W., Powell, R., & Holland, T. J. B. (2007). Progress relating to calculation of partial melting equilibria for metapelites. *Journal of Metamorphic Geology*, *25*(5), 511–527. https://doi.org/10.1111/j.1525-1314.2007.00711.x

White, R. W., Powell, R., Holland, T. J. B., Johnson, T. E., & Green, E. C. R. (2014). New mineral activity-composition relations for thermodynamic calculations in metapelitic systems. *Journal of Metamorphic Geology*, *32*(3), 261–286. https://doi.org/10.1111/jmg.12071

White, R. W., Powell, R., Holland, T. J. B., & Worley, B. (2000). The effect of TiO_2 and Fe_2O_3 on metapelitic assemblages at greenschist and amphibolite facies conditions: Mineral equilibria calculations in the system K_2O–FeO–MgO–Al_2O_3–SiO_2–H_2O–TiO_2–Fe_2O_3. *Journal of Metamorphic Geology*, *18*, 497–511. https://doi.org/10.1046/j.1525-1314.2000.00269.x

White, R. W., Powell, R., & Johnson, T. E. (2014). The effect of Mn on mineral stability in metapelites revisited: New a-x relations for manganese-bearing minerals. *Journal of Metamorphic Geology*, *32*(8), 809–828. https://doi.org/10.1111/jmg.12095

Whittington, A. G., Hofmeister, A. M., & Nabelek, P. I. (2009). Temperature-dependent thermal diffusivity of the Earth's crust and implications for magmatism. *Nature*, *458*, 319–321. https://doi.org/10.1038/nature07818

SUPPORTING INFORMATION

Additional supporting information may be found online in the Supporting Information section at the end of the article.

Appendix S1. Finite-difference radiogenic heat-production and lithospheric heat-conduction models.

Appendix S2. Emplacement temperatures of the Anosyen Batholith.

Appendix S3. Reference materials and reduction of LASS monazite and zircon data.

Figure S1. Th and Y maps of monazite from leucocratic segregations in sample 23A.

Figure S2. Weight fraction silicate melt *v.* temperature calculated in rhyoliteMELTS for seven charnockites bulk compositions from the Anosyen Batholith.

Table S1. Sample locations.

Table S2. EPMA mineral analyses.

Table S3. Feldspar thermometry inputs.

Table S4. Bulk-rock compositions for pseudosections.

Table S5. LASS zircon data.

Table S6. LASS monazite data.

Table S7. Thermal model parameters.

Table S8. Bulk compositions of orthopyroxene granites for rhyoliteMELTS.

How to cite this article: Holder RM, Hacker BR, Horton F, Rakotondrazafy AFM. Ultrahigh-temperature osumilite gneisses in southern Madagascar record combined heat advection and high rates of radiogenic heat production in a long-lived high-*T* orogen. *J Metamorph Geol*. 2018;36: 855–880. https://doi.org/10.1111/jmg.12316